Tire lateral force estimation and grip potential identification using Neural Networks, Extended Kalman Filter, and Recursive Least Squares

Acosta, M & Kanarachos, S

Original citation & hyperlink:
Acosta, M & Kanarachos, S 2017, 'Tire lateral force estimation and grip potential identification using Neural Networks, Extended Kalman Filter, and Recursive Least Squares' *Neural Computing and Applications*, vol (in press), pp. (in press)
https://dx.doi.org/10.1007/s00521-017-2932-9

DOI 10.1007/s00521-017-2932-9
ISSN 0941-0643
ESSN 1433-3058

Publisher: Springer

The final publication is available at Springer via http://dx.doi.org/10.1007/s00521-017-2932-9

Tire lateral force estimation and grip potential identification using Neural Networks, Extended Kalman filter, and Recursive Least Squares

Manuel Acosta[1] · Stratis Kanarachos[2]

Email[1]: ac3354@coventry.ac.uk

Phone: +44 (0)7 492 18 89 02

Email[2]: ab8522@coventry.ac.uk

School of Mechanical, Aerospace and Automotive Engineering, Coventry University, United Kingdom.

Abstract This paper presents a novel hybrid observer structure to estimate the lateral tire forces and road grip potential without using any tire-road friction model. The observer consists of an Extended Kalman Filter structure, which incorporates the available prior knowledge about the vehicle dynamics, a feedforward neural network structure, which is used to estimate the highly non-linear tire behavior, and a Recursive Least Squares block, which predicts the road grip potential. The proposed observer was evaluated under a wide range of aggressive maneuvers and different road grip conditions using a detailed validated vehicle model, validated tire model and sensor models in the simulation environment *IPG CarMaker*®. The results confirm its good and robust performance.

Keywords Tire force estimation·Grip potential estimation·Neural Networks·Hybrid observer

1. Introduction

Lateral dynamics estimation has been an extensive field of automotive research during the last decades. As [1] pointed out, the influence of driver actions on the chassis responses, i.e. *controllability*, is strongly influenced by the vehicle sideslip, which depends directly on the tire-road friction interaction. Thus, in order to keep the vehicle within controllable and stable limits, active safety systems limit the vehicle's sideslip angle. On the other hand, latest research results suggest that collision avoidance in some situations might be possible only if high attitudes angles are generated, e.g. *drift* [2,52], so it is expected that accurate lateral dynamics estimation in aggressive maneuvers will be required to apply these *Advanced Driver Assistance Systems* (*ADAS*) solutions. Unfortunately, the stochasticity and nonlinearity with the forces generated by the tires as well as the road grip coefficient contribute to complicating significantly this task.

Different approaches have been proposed in the literature for estimating in real-time the tire forces. The most extended among them is the well-known Kalman Filter [3–7]. To start with, [3, 7] suggested an Extended Kalman Filter (*EKF*) structure where the tire-road interactions were modeled using a *Dugoff* tire model. In [3], the grip coefficient was treated as a stochastic variable while in [7] was considered a known parameter. Both designs were validated at constant speed tests. *EKF* is most suitable for smooth nonlinear problems and cannot handle highly nonlinear problems [7]. In an attempt to estimate tire forces during aggressive maneuvers, [8] presented an Unscented Kalman Filter (*UKF*) based on a detailed vehicle model which included the Magic Formula empirical model to estimate the tire-road interactions. Road grip was modeled as a stochastic variable and results were presented in ABS braking maneuvers and sine steer tests. Other authors [9, 10] tried to approximate the tire-road interactions by using Sliding Mode Observation (*SMO*) techniques. In [10] a linear adaptive tire model was proposed. These methods were validated in constant speed maneuvers. Finally, [4, 11, 12] eliminated completely the tire modeling task, and considered the tire forces as stochastic variables, using a random-walk Kalman Filter approach.

This *tire model-less* trend has been accepted and followed by other authors. [13, 14] pursued the estimation of tire forces from standard inertial measurements using simple methods such as RLS or PID observers. [15] Integrated successfully vertical forces and shaft torque estimation modules to predict the tire forces under combined solicitations (longitudinal and lateral traction). In [16], online lateral force measurements from load-sensing hub bearings were presented and used to estimate the vehicle lateral velocity. In [49] the tire forces were estimated using an optical tire sensor. In the same line of thought, some authors took a different path and focused on kinematic models to achieve an accurate lateral dynamics estimation. [17] described a kinematic observer based on *GPS* and Inertial Motion Unit sensor fusion, [18] used *GPS* information to develop a motorsport observer for high attitude angles and [19] presented a robust approach using a Domain Control Unit with 6- Degrees Of Freedom *(DOF)* of the vehicle body. The main problem encountered with kinematic observers is the signal drift over a prolonged period of observation when no reference signal exists.

Other authors tried to solve the problem from a different perspective, by following a data-based approach instead of a tire model-based. Thus, [20] proposed a "black-box" approach to model the lateral dynamics using feedforward and recurrent Neural Network *(NN)* structures. Results were shown for steady state and lane change maneuvers under different road grip conditions. Similarly, [21] used the "black-box" concept and generated a training dataset using random steering inputs at constant speed. The structure was tested in lane change maneuvers.

While the adherence coefficient was considered an a priori known parameter in the majority of the works presented in the preceding paragraphs, other authors [22–26], have studied the identification of this parameter in detail. Concerning lateral slip-based approaches, in [23], relevant work was presented using Multibody simulation tools and an off-line road grip identification method based on Genetic Algorithms and lateral acceleration error. These works were completed in [24], where an on-line estimator was presented using an *EKF* and an *NN* structure. The latter was proposed as an efficient and simple way to handle the correlation between tie-rod forces and tire self-alignment moment. The same concept, based on the *tire self-alignment moment* information, was exploited in [22, 25]. In [25] Torque measurements from the Electric Power Steering system (EPS) were used to predict the lateral grip margin, while in [22] an online identification method using strain gauge measurements on the steering tie rods was presented. Other authors [48] have focused on the grip recognition based on longitudinal slip-based methods. Finally, the *Smart Wheel* was presented in [26] as an accurate way to supply the tire forces and self-alignment moments required for the road friction identification.

In this paper, a *tire model-less* approach is presented taking advantage of a novel hybrid observer structure. The proposed methodology is fundamentally different compared to other approaches, in the sense that it does not assume an a priori knowledge of the tire model nor does it treat the vehicle dynamics as a black box. Instead, it combines the advantages of Neural Networks in modeling the tire's highly nonlinear behavior using a data-based approach with a first principles vehicle model that captures the overall dynamic behavior. In particular, the vehicle planar dynamics are modeled using an *EKF* based on a 3-DOF vehicle model and the tire-road interactions are estimated by a Feedforward *NN* structure. The *NN* structure is formed by the high grip (high mu), intermediate grip (mid mu) and low grip (low mu) blocks. Information from these blocks is fed into a Recursive Least Squares (*RLS*) module to complete the road grip potential identification process. The grip estimator block proposed in this paper is developed considering the road as a rigid surface, (e.g. asphalt, wet asphalt, ice), that is, assuming that the road friction in low adherence conditions can be approximated using a scaling approach such as described in [28]. Surfaces such as gravel, sand or loose snow are considered out of the scope of this research due to the complexity derived from the tire friction mechanisms. Additionally, road grade and road bank angle are disregarded, assuming that the road is completely flat. The modular structure of the estimator permits the addition of an external observer developed for this task without a considerable burden (e.g. kinematic-based [ref]).

This state estimator presents an inherent advantage with respect to other works found in literature [7], as it takes into consideration the influence of the longitudinal dynamics on the tire force generation. This extends the operating range of the observer to non-constant-speed maneuvers such as braking in a turn or power off. Thus, the approach described in this paper is proposed as an efficient way to recognize the road grip potential under intermediate driving situations, where neither pure lateral slip-based nor longitudinal slip-based methods provide accurate results due to lack of dynamic excitation (i.e. grip consumption level) or force coupling (i.e. combined efforts in the longitudinal and lateral direction). These blocks can be integrated forming a hybrid structure [53], where the output from each estimator is weighted according to the driving situation.

In Section 2, the vehicle model and tire-force prediction block are presented. A description of the observer structure is included in Section 3, followed by a brief insight into the Discrete Extended Kalman Filter, Feedforward Neural Networks, and Recursive Least Squares formulation. Detailed explanations about the Neural Networks training, grip identification block, and observer implementation complete the content of the Section. Results are presented in Section 4 for different open loop, closed loop and mu-jump maneuvers implemented in *IPG CarMaker®*, to evaluate the performance of the observer. The robustness of the state estimator is tested under variations in the tire size and tire operating pressure. Finally, Section 5 includes a discussion of the results and further research steps are proposed.

2. Vehicle Modeling

A single track model is used to capture the vehicle planar dynamics, Fig. 1. Despite the simplicity of this model, satisfactory results have been obtained in previous works [4, 9, 10], demonstrating that this approach represents a good compromise between model complexity and accuracy of results. The dynamic equations were discretized using a First order approximation ($e^{AT_s} \approx 1 + AT_s$) and expressions (1-3) were obtained.

$$v_{x,k+1} = v_{x,k} + r_k v_{y,k} + \frac{T_s}{m}\left(F_{xf,k}\cos(\delta_k) - F_{yf,k}\sin(\delta_k) + F_{xr,k}\right) \quad (1)$$

$$v_{y,k+1} = v_{y,k} - r_k v_{x,k} + \frac{T_s}{m}\left(F_{yf,k}\cos(\delta_k) + F_{xf,k}\sin(\delta_k) + F_{yr,k}\right) \quad (2)$$

$$r_{k+1} = r_k + \frac{T_s}{I_z}\left(F_{yf,k}\cos(\delta_k)l_f + F_{xf,k}\sin(\delta_k)\,l_f - F_{yr,k}l_r\right) \quad (3)$$

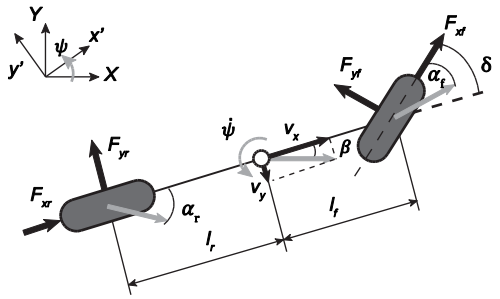

Fig. **1** Single Track model

In this paper, the steering wheel angle δ is considered an input variable to the system, which can be obtained from the signals available in the vehicle *CAN* bus. The vehicle mass m, yaw inertia I_z, and distances from the front and rear axle to the center of gravity l_f, l_r, are assumed to be known constant parameters. A robustness analysis was performed to check that this assumption was valid under normal weight variations (kerb – 2 passengers). The estimation of the longitudinal forces F_{xf}, F_{xr} is out of the scope of this paper. These are treated as inputs to the system that can be estimated by an external observer using Engine Management Torque signals and *ESP* brake pressure measurements [27]. Finally, the state vector is formed by the yaw rate r_k, the longitudinal velocity v_x and the lateral velocity v_y. The output states (measurable variables) are the yaw rate and the longitudinal velocity.

$$U_k = (\delta_k, F_{xf,k} F_{xr,k}) \quad (4)$$
$$Y_k = (r_k, v_{x,k}) \quad (5)$$
$$X_k = (r_k, v_{x,k}, v_{y,k}) \quad (6)$$

2.1. Tire model

The tire lateral forces are assumed to be unmeasurable signals that depend on the vehicle states. These forces are estimated at each time step by the Neural Network structure, assuming a quasi-static model of the form (7, 8).

$$F_{yf,k} = f(\alpha_{f,k}, \lambda_k) \quad (7)$$
$$F_{yr,k} = f(\alpha_{r,k}, \lambda_k) \quad (8)$$

Where α represents the tire lateral slip and λ the tire longitudinal slip. The expressions (7, 8) are often approximated using an analytical or empirical static tire model, e.g. Magic Formula [28]. Tire dynamics are added by means of the relaxation length, and a first order low pass filter structure is proposed as an acceptable approximation [7]. For further discussion in tire transient dynamics, the reader is referred to [29].

$$F_y \approx F_{y0} + \frac{\partial F_y}{\partial \alpha}(\Delta\alpha) + \frac{\partial F_y}{\partial \lambda}(\Delta\lambda) \quad (9)$$

As a *tire model-less* approach is proposed in this work, no previous knowledge about the non-linear tire-road interactions is assumed. Thus, functions (7, 8) are linearized using a first order Taylor expansion (9), Fig. 2. The equilibrium term F_{y0} is estimated directly from the Neural Network block. The derivative of the lateral force $\frac{\partial Fy}{\partial \alpha}$ is calculated using a finite difference approximation (10). The term $\Delta\alpha_t$ is a fixed increment used in equation (10) and thus is independent from the $\Delta\alpha$ of expression (9).

$$\frac{\partial F_y}{\partial \alpha} = C \approx \frac{F_{y,\alpha_0+\Delta\alpha_t} - F_{y,\alpha_0-\Delta\alpha_t}}{2\Delta\alpha_t} \quad (10)$$

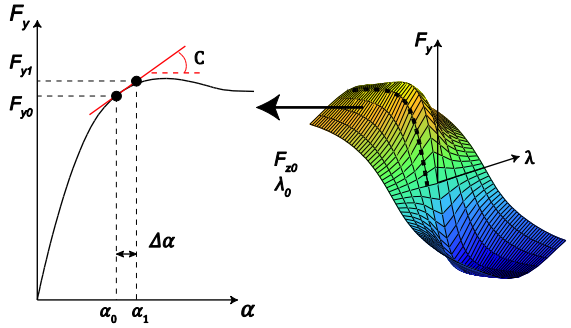

Fig. 2 Linear approximation of tire lateral force for a given nominal load (F_{z0}) and longitudinal slip (λ).

The second derivative term ($\Delta\lambda$) is neglected under the assumption of quasi-static conditions in the longitudinal direction [30]. In other words, the braking and driving commands are considered steady-state events in comparison to the driver steering corrections. Tire dynamics are considered of little influence in the planar dynamics chassis operating range (0-5Hz), [31]. Finally, the wheel slips are related to the system states by the expressions (11, 12) using a small angle assumption [32].

$$\alpha_{f,k} = \delta_k - \left(\frac{r_k l_f + v_{y,k}}{v_{x,k}}\right) \quad (11)$$
$$\alpha_{r,k} = -\left(\frac{v_{y,k} - r_k l_r}{v_{x,k}}\right) \quad (12)$$

3. Observer Structure

The structure of the observer presented in this paper is depicted in Fig 3. As can be noticed, a hybrid structure [33] formed by an *EKF*, *NN* structure and *RLS* block is proposed.

Table 1. Observer inputs and outputs

Signal	EKF	NN	RLS
Inputs	δ, F_{xf}, F_{xr}	α, a_x	$F_{yf,high-mid-low}$
Measurements	r, v_x	-	-
Outputs	$\hat{r}, \hat{v}_x, \hat{v}_y$	$F_{yhigh-mid-low}$	$\hat{\mu}$

This modular approach has significant advantages with respect to the standard *NN* "black-box" modeling, as it combines an a priori knowledge of the process being modeled (Planar dynamics - *EKF*) with an estimation of the unknown parameters (Tire forces - Neural Network, Grip coefficient - *RLS*). As portrayed in Fig 3, the states predicted by the *EKF* in the *Time Update* step are used to estimate the axle wheel slips. These values are used as inputs in addition to the longitudinal acceleration in the *NN high-mid-low mu* blocks.

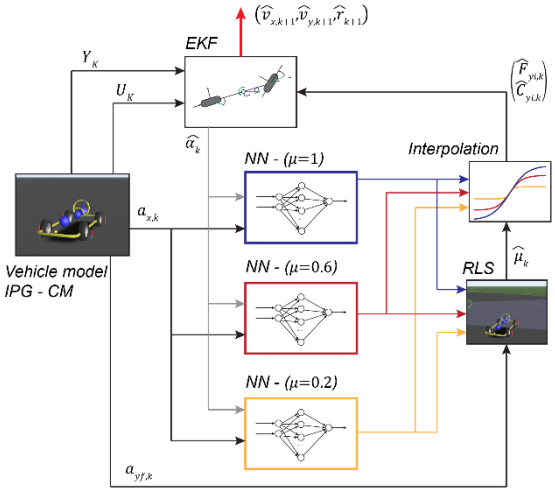

Fig. 3 Hybrid observer structure diagram.

The *NN* outputs feed the *RLS* block, in which the road grip coefficient is estimated. The tire forces are linearly interpolated on the basis of the estimated grip and reinjected into the *EKF* block. Finally, the *EKF* corrects the vehicle states using the yaw rate and longitudinal velocity measurements in the *Measurement Update* stage. Table 1 summarizes the signals used at each observer block.

3.1. Discrete Extended Kalman Filter

The *EKF* is presented using the state space formulation. A nonlinear dynamic system is described by the set of discrete equations (13, 14):

$$X_{k+1} = f(X_k, U_k) + w_k \quad (13)$$
$$Y_k = h(X_k) + v_k \quad (14)$$

Where $f(.)$ and $h(.)$ represent the state evolution and observation vectors, X_k, U_k the system states (yaw rate r_k, long. velocity v_x and lat. velocity v_y) and system inputs (steering angle δ, front long. force F_{xf} and rear long. force F_{xr}) respectively and Y_k the observed variables. The process uncertainties and observation noises are modeled by the variables w_k and v_k. These are assumed to be Gaussian, uncorrelated and zero mean, i.e. $(w \approx N(0, Q), v \approx N(0, R))$. Q and R are referred as the filter tuning covariance matrices. Following the formulation presented in [7] the *EKF* filter function is represented by the expressions (15-19).

Time update

$$\hat{X}_{k|k-1} = f(\hat{X}_{k-1|k-1}, U_k) \quad (15)$$
$$P_{k|k-1} = A_k P_{k-1|k-1} A^T + Q \quad (16)$$

Measurement update

$$K_k = P_{k|k-1} H_k^T [H_k P_{k|k-1} H_k^T + R]^{-1} \quad (17)$$
$$\hat{X}_{k|k} = \hat{X}_{k|k-1} + K_k [Y_k - h(\hat{X}_{k|k-1})] \quad (18)$$
$$P_{k|k} = [I - K_k H_k] P_{k|k-1} \quad (19)$$

During the *Time update* stage, the system states are predicted according to the process model (a priori knowledge of the system). The predicted covariance matrix $P_{k-1|k-1}$ is calculated using the process covariance matrix Q and the Jacobian matrix A_k of the state evolution vector $f(\cdot)$. After that, in the *Measurement update* stage, the system states are corrected according to the measurement residuals using the filter gain K_k and the covariance matrix of the next step is computed $P_{k|k}$. In order to determine whether the system states can be estimated from the available set of measurements it is necessary to study the observability of the system. If a Taylor-expansion of the expression (14) is developed with respect to time, the equation (20) is obtained, [34].

$$y(t) \approx y(0) + t\dot{y}(0) + \frac{t^2}{2!}\ddot{y}(0) + \cdots + \frac{t^{n-1}}{(n-1)!} y^{n-1}(0) \quad (20)$$

Where n denotes the number of states of the system. The first time derivative can be presented as a function of the state evolution vector using the chain rule (21).

$$\begin{aligned} \dot{y} &= \frac{\partial h}{\partial t} \\ &= \frac{\partial h}{\partial x} \cdot \frac{\partial x}{\partial t} \\ &= \frac{\partial h}{\partial x} f(X, U) \end{aligned} \quad (21)$$

In order to simplify the calculation of the higher order terms, the Lie Derivative operator is taken (22).

$$L_f \cdot h_i = \frac{\partial h_i}{\partial x} f(X, U) \quad (22)$$

Here i represents the i-th term of the observation vector h. The higher order derivative terms can be expressed recursively (23), with the initial condition (24), where r denotes the (n-1)-th derivative with respect to time, $r = 1 \ldots n-1$.

$$L_f^r \cdot h(X) = L_f \left(L_f^{r-1} \cdot h(X) \right) \quad (23)$$
$$L_f^0 \cdot h(X) = h(X) \quad (24)$$

Thus, the derivative terms required to describe the output of a dynamical system can by grouped in matrix form (25).

$$\begin{pmatrix} y \\ \dot{y} \\ \dots \\ y^{n-1} \end{pmatrix} = \begin{pmatrix} L_f^0 \\ L_f^1 \\ \dots \\ L_f^{n-1} \end{pmatrix} \cdot h(X) \tag{25}$$

The system will be locally observable if the states can be reconstructed from the available measurements. To study this, it is necessary to linearize the system outputs around the equilibrium states (x_0) by a first order Taylor-expansion (26).

$$y^r \approx h(x_0) + \frac{\partial h}{\partial x}(x - x_0) \tag{26}$$

Then, the local observability will be guaranteed if expression (26) is invertible. If all the derivative terms are grouped, the local observability analysis is reduced to study the rank of the nonlinear observability matrix, O (27).

$$O = \begin{pmatrix} L_f^0 \\ L_f^1 \\ \dots \\ L_f^{n-1} \end{pmatrix} \cdot \frac{\partial h}{\partial x} \tag{27}$$

$$\Lambda(X_k) = \frac{\lambda_{min}[O^T O, X_k]}{\lambda_{max}[O^T O, X_k]} \tag{28}$$

An efficient way to evaluate the *degree* of local observability of the system [7, 10] is to study the conditioning ratio of the observability matrix. The conditioning ratio is defined by the ratio of the minimum and maximum eigenvalues of the observability matrix (28). The system analyzed in this paper is observable unless the longitudinal velocity is zero. In order to avoid ill-conditioning, the system is switched off each time the vehicle velocity goes below the 2.7 m/s threshold (29).

$$X_k = \begin{cases} X_k, & v_x > 2.7\ m/s \\ 0, & v_x \leq 2.7\ m/s \end{cases} \tag{29}$$

3.2. Feedforward Neural Networks

Feedforward Neural Networks are used to characterize time-independent properties of systems. The formal description of static systems is given in (30), [35].

$$Y_k = f(U_k, Z_k) \tag{30}$$

Where Y_k is the output vector of the system, U_k is the input vector and Z_k comprises the system parameters. The simplest element of a Neural Network Structure is an Artificial Neural Network cell (Neuron), Fig. 4.

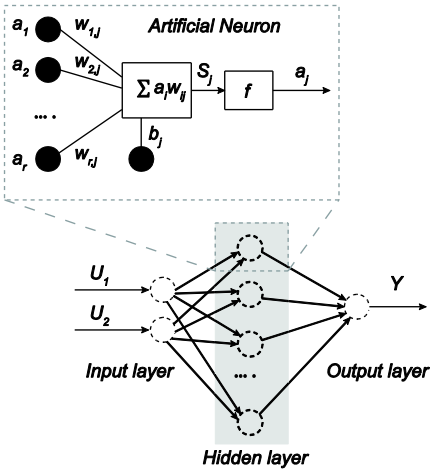

Fig. 4 Neural Network Structure and Artificial Neural Network cell.

Neurons are grouped forming a structure of different layers, named Input layer, Hidden Layers, and Output Layer. Between the input and output layers, a series of simple operations are performed, given by the equations (31, 32).

$$S_j = \sum_i w_{ij} a_i + b_j \tag{31}$$

$$a_j = f(S_j) \tag{32}$$

Where S_j represents the output from the j^{th} neuron, formed by the sum of the relevant products of weights (w_{ij}) and outputs (a_i) from the previous layer i. This sum is biased by the factor b_j. a_i represents the activation of the node at hand and f the activation function of the j layer. Normally, sigmoid functions are chosen for the hidden layers while linear functions are set for the output layers.

3.2.1. Neural Network Structure

Axle lateral forces are modeled using a Feedforward Neural Network Structure. In order to keep the complexity of the *NN* structure low, the number of hidden layers was set to one prior to starting with the selection of the number of internal neurons. After a sensitivity analysis in which different number of hidden neurons were tested, a structure formed by ten hidden neurons was selected (1-10-1). As good results were obtained with a single hidden layer, it was not necessary to repeat the sensitivity analysis with additional layers. The inputs to the static *NN* structure are the axle wheel slip (α_i) and the measured longitudinal acceleration (a_x). This approach is contrary to the traditional formulation of quasi-static tire models (7, 8), [28] where in addition to the wheel slip angle, tire nominal forces and tire longitudinal slip are required (33).

$$F_y = f(F_z, \alpha, \lambda) \tag{33}$$

Without considering the burden of accurately estimating wheel longitudinal slips and tire nominal loads, training a

Neural Network structure with this number of inputs will add a notable complexity to the problem. Thus, in this paper, a simple but efficient approach is used under the following considerations:

Quasi-static weight transfer: If suspension pitch dynamics are neglected, axle vertical loads can be expressed as a function of the longitudinal acceleration (34).

$$F_{z,i} = F_{zest,i} \mp \frac{mh_{CoG}}{(l_f + l_r)} a_x, \quad i = \{f, r\} \tag{34}$$

Axle adherence ellipsoid: While operating in the longitudinal linear region, axle longitudinal forces can be expressed as a function of the vehicle longitudinal acceleration. Under braking events, this function will depend on the braking bias, while in driving circumstances the axle longitudinal forces will vary according to the driveline layout. (35).

$$\begin{aligned} F_{xi} &= f_{brk}(a_x), \quad a_x < 0 \\ F_{xi} &= f_{drive}(a_x), \quad a_x > 0 \end{aligned} \tag{35}$$

The effect of these relationships can be observed in Fig 5. These graphs are equivalent to the ellipse of adherence of each axle. Concerning the front axle, Fig. 5 (a), the maximum lateral force remains almost constant up to $-4\ m/s^2$. While the maximum lateral force decreases with the braking force, (due to the force coupling effect), the positive weight shift derived from the braking action increases the total force available (these effects cancel each other in gentle decelerations).

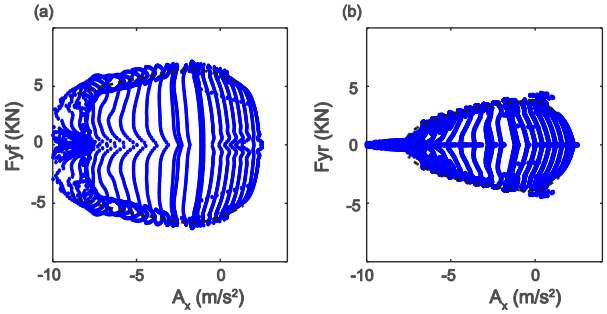

Fig. 5 (a) Front axle adherence ellipse. (b) Rear axle adherence ellipse.

On the other hand, the lateral force of the rear tires, Fig. 5 (b), diminishes abruptly with the longitudinal deceleration. In this case, apart from the lateral force reduction caused by the braking action, a negative load transfer occurs, and the maximum force available on the tire is reduced. The axle lateral forces are a function of the longitudinal acceleration a_x and axle wheel slips α. Thus, in this paper the expression (33) is reformulated as (36).

$$F_y = f(F_z, \alpha, \lambda) \approx f(a_x, \alpha) \tag{36}$$

3.2.2. Neural Networks Training

Several maneuvers were considered to train the *NN* structure, Table 2. Preferably, these tests should guarantee repeatability and be easy to perform.

In addition, they should provide data from the tire nonlinear region. This is of vital importance to training the *NN* for accurate prediction during aggressive maneuvers. Based on the authors' experience in chassis characterization and vehicle dynamics testing, steady-state maneuvers were avoided during the training stage due to the low range of rear axle wheel slip covered (-5, 5) deg. Closed loop maneuvers were avoided during the training stage due to the poor repeatability and reduced longitudinal acceleration range covered.

Table 2. Handling Maneuvers

Notation*	Wheel slip range [Front / Rear]	Longitudinal range [m/s2]	Repeatability
SIS	High / Low	(≈ 0)	High
SSR	High / Low	(≈ 0)	High
FR	Low / Low	(≈ 0)	High
ISO LC	High / High	(0, -2)	Low
SL	High / Low	(≈ 0)	Low
DS	High / Low-High	(0, -2)	High
SST	High / Low-High	(0,-2)	High
SST-Drv	High/Low	(0,4)	High
SST-Brk	High/High	(0,-10)	High

*SIS: Slow Increasing Steer, *SSR: SS const. radius, *FR: Frequency Response, * ISO-LC: ISO Lane change, *SL: Slalom, *DS: Sine with Dwell, *SST: Step steer, *SST-Drv: Power on Step steer, *SST-Brk: Braking Step steer.

Finally, step steer tests including its longitudinal variants (Power on and Braking) were selected. These maneuvers can be performed manually or with a Steering Robot [31, 36], and can provide a wide range of data along the tire nonlinear region. Since these extreme maneuvers are hard to perform by a regular driver, the applicability of the proposed method is restricted. More specifically, the envisaged application domain is the automated development of estimators/ controllers using steering robots. The training datasets were generated using the vehicle dynamics simulation software *IPG-CarMaker®*. The vehicle model used and test conditions are specified in Table 3.

Table 3. Car Maker model

Vehicle	Fiesta_exp
Tires	MF 6.1 205_65/R16
Nominal tire pressure:	2.4 bar
Max. SWR	200 deg/s
Grip	Low mu: 0.2 / Mid mu:0.6 / High-mu:1

The maximum steering velocity during the generation of the training datasets was set to 200 deg/s. Despite a driver can achieve peak values as high as 1100 deg/s during an emergency maneuver [54], the steering frequency rarely exceeds the 0.4-0.5 Hz threshold during normal driving situations [54]. Assuming a maximum rotation amplitude of 80-90 degrees at this frequency (160-180 degrees peak-to-peak), a maximum steering rate of

200 deg/s can be considered for regular driving situations. Accurate results were obtained during the evaluation of the observer under aggressive maneuvers involving faster steering inputs (up to 1000 deg/s), Section 5.

The vehicle model *Fiesta_exp* was generated after characterizing the instrumented vehicle depicted in Fig. 6. The tire behavior was modeled using a state-of-the-art tire model (Magic Formula 6.1, [28]). The size of the tire model is detailed in Table 3. This tire model incorporates the influence of the tire inflation pressure on the friction forces and uses a relaxation length approach to model the tire dynamics. The tire model was characterized in a high adherence ($\mu \approx 1$) surface. Tire experimental results in low adherence surfaces were not available for this specific tire model, and thus the training datasets in low mu conditions were generated employing the scaling approach described in [28]. Additional experiments to corroborate this scaling approach using experimental data from a sedan-like tire are included in Section 4.5.

In order to corroborate the validity of the simulation model, steady-state and lane change maneuvers were executed with the experimental vehicle and results were compared to the simulation outputs. The steering inputs acquired through the *CAN* of the vehicle were fed into the simulation model, and a *PID* controller was used to regulate the vehicle reference velocity (acquired with GPS).

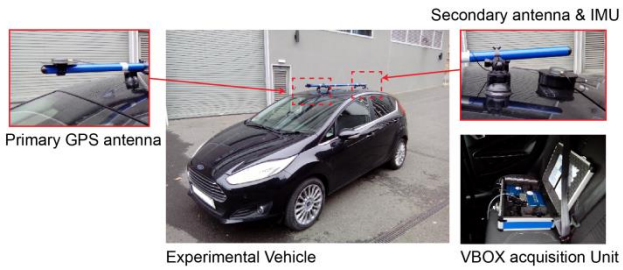

Fig. 6 Ford Fiestainstrumented vehicle.

The testing equipment used during the experimental tests is detailed in Table 4. A number of CAN signals are available including engine speed, engine torque, steering angle, throttle braking pedal position, wheel speeds, yaw rate, longitudinal and lateral acceleration. All measurements were post-processed offline. The lateral acceleration was translated from the IMU position to the center of gravity, and the signals were low-pass filtered using an 8th order Butterworth filter with a cut-off frequency of 8Hz.

Table 4. Vehicle instrumentation

GPS:	RaceLogic Dual Antenna
IMU:	RaceLogic RLVBIMU04
Acquisition Unit:	RaceLogic VBOX 3i
CAN:	Connection through EOBD port
Acquisition frequency:	100 Hz

As can be observed in Figures 7 and 8, the experimental results correlate well with the outputs obtained from the simulation model.

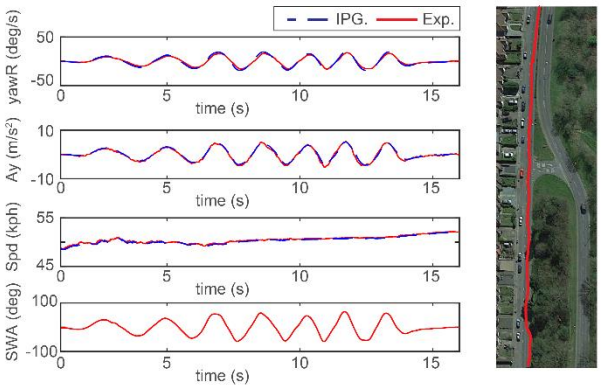

Fig. 7 Lane change test performed with the experimental vehicle.

Once the simulation model was validated, the training datasets were generated. Lateral forces were saved after each simulation and concatenated forming the *NN* output vector. Alternatively, these can be reconstructed from other vehicle states [4]. The same process was followed with the longitudinal acceleration and axle sideslip angles in order to construct the *NN* input vector. Raw training datasets can be seen in Fig. 5 and Fig. 11 (a).

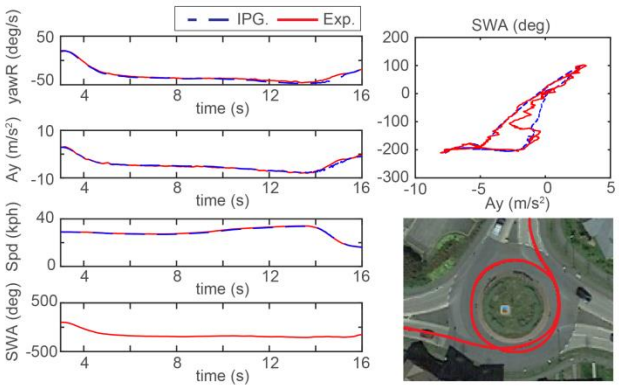

Fig. 8 Steady-state test performed with the experimental vehicle.

The Neural Networks were constructed and trained in *Matlab*® using the Neural Network toolbox [37]. As mentioned in the previous section, a one-hidden-layer structure composed by ten neurons (1-10-1) and sigmoid activation functions was employed. In order to study the stability of the *NN* [35], the training process was repeated several times using different initial weights. Groups of 20, 50 and 100 Neural Networks were generated and the average output of these structures was used as the most probable value for the estimated lateral force [35]. As can be noticed in Fig. 9 (a), little difference is observed between the outputs of the three groups ($N = 20, N = 50, N = 100$). Different training methods were evaluated (Bayesian Regularization BR, and Levenberg-Marquardt LM) and three different dataset divisions were tested (70/15/15, 60/20/20, and

90/5/5). Almost identical values were obtained regardless of the training method or the dataset division, Fig. 9 (b).

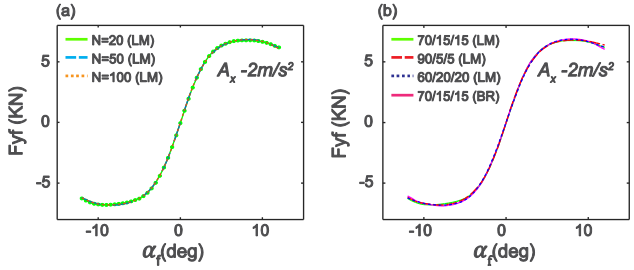

Fig. 9 (a) NN average output for groups of different size. (b) NN output for different training methods and dataset divisions.

In order to minimize the training time, the Levenberg-Marquardt Backpropagation algorithm was finally used (Bayesian Regularization may be better for challenging problems but requires higher computational resources [37].). The dataset division was set to the *Matlab*® Neural Network toolbox default (70/15/15), as no relevant differences were noticed when testing other dataset divisions.

Finally, with the aim to have good accuracy but avoid high computational cost, an average was taken from the 20 structures and the structure showing minimum dispersion with respect to the average value was implemented in the final observer.

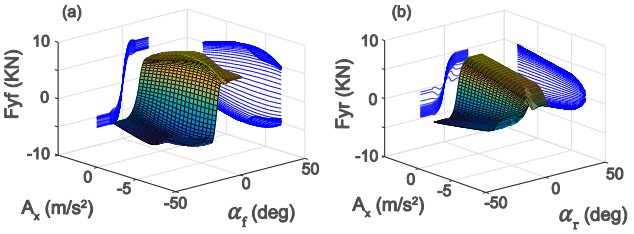

Fig. 10 (a) Neural Networks output, Front axle. (b) Neural Networks output, Rear axle.

In Fig. 10. outputs from the final Neural Networks under a combination of longitudinal acceleration and wheel slip inputs are depicted. Graphs show smooth and symmetrical surfaces. In addition, the characteristic ellipse shape described in the previous subsection can be noticed.

3.2.3. Modeling tire forces in low adherence

In order to provide a reliable estimation of the tire forces under low adherence conditions, it is necessary to capture the tire responses in these surfaces. A straightforward approach would suggest to include the estimated grip coefficient $\hat{\mu}$ as an additional input to the Neural Network structure. This solution could provide accurate results for adherence coefficients close to those included in the training dataset, Fig 11 (a). Nevertheless, this could lead to unpredictable outputs as soon as the grip coefficient differs slightly from the original training dataset, Fig 11 (b).

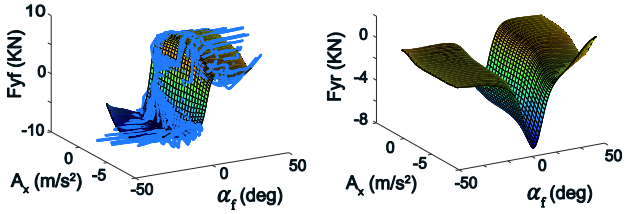

Fig. 11 (a) Neural Network output, ($\mu = 1$). (b) Neural Network output ($\mu = 0.95$).

To avoid this, a *divide and conquer* approach is used. The training process described previously is repeated in two additional surfaces: mid mu ($\mu = 0.6$) and low mu ($\mu = 0.2$). The tire friction in these surfaces is simulated using the grip scaling approach employed by the *Magic Formula 6.1* [28]. A comparison between the tire forces obtained using this scaling approach and those measured experimentally in low mu surfaces is included in Section 4.5.

The outputs from the three structures ($F_{yhigh}, F_{ymid}, F_{ylow}$) are interpolated according to the estimated grip coefficient ($\hat{\mu}$) using a linear relationship (39-44). The entire set of possible grip coefficients is considered a closed interval that goes from $\mu = 1$ to $\mu = 0.2$. Despite higher grip coefficients may be present in some situations (e.g. *motorsport*), these are not covered in this paper, and thus the analysis of the state estimator is limited to the adherence coefficients included in this interval. A segmentation approach is employed and two interpolation intervals are defined (37-38):

$$I_1 = \{\hat{\mu}, 0.6 \leq \hat{\mu} \leq 1\} \quad (37)$$

$$I_2 = \{\hat{\mu}, 0.2 \leq \hat{\mu} < 0.6\} \quad (38)$$

If the estimated grip coefficient is higher than 0.6, the grip is located in the first interval (I_1), and the upper interpolation surfaces (high-mid mu) are used (39-41):

$$\hat{F}_{yi} = c_1 F_{yi,high} + c_2 F_{yi,mid} \quad (39)$$

$$c_1 = a_1\hat{\mu} + a_2 \quad (40)$$

$$c_2 = b_1\hat{\mu} + b_2 \quad (41)$$

Otherwise, if $\hat{\mu}$ is below the 0.6 threshold, the mid and low mu surfaces are employed (42-44):

$$\hat{F}_{yi} = c_3 F_{yi,mid} + c_4 F_{yi,low} \quad (42)$$

$$c_3 = a_3\hat{\mu} + a_4 \quad (43)$$

$$c_4 = b_3\hat{\mu} + b_4 \quad (44)$$

The coefficients are adjusted to satisfy the boundary conditions $\mu = 1$, $\mu = 0.6$ and $\mu = 0.2$.

Remark: In this paper, smooth surfaces are considered, i.e. asphalt, wet asphalt, ice, etc. Off-road surfaces such as sand or

deep snow present a high degree of complexity (e.g. bulldozing effects) and are out of the scope of this paper. For further details [38–40] can be reviewed.

3.3. Recursive Least Squares

The grip coefficient ($\hat{\mu}$) required to estimate the tire forces is obtained using a *RLS* module. *RLS* is often used in online identification tasks to minimize the error caused by different sensor noises [6, 14]. The measured output (y_k) is related to the estimated parameter (θ_k) using the expression (45), where (ψ) is the input regression term.

$$y_k = \psi^T \theta_k \tag{45}$$

At each time step, the difference between the current measurement and the last prediction is minimized (46). The gain and covariance terms are obtained through (47, 48). The exponential factor (λ) is used to diminish the relative weight of the last estimates on the predicted step. Smaller values are used to assign less weight to previous estimates [41]. By tuning the exponential factor, a good trade-off between noise filtering and parameter adaptation can be achieved (See subsection 3.3.1 for additional details regarding the tuning of the forgetting factor).

$$\hat{\theta}_{k+1} = \hat{\theta}_k + K_{k+1}\left(y_{k+1} - \psi_{k+1}^T \hat{\theta}_k\right) \tag{46}$$
$$K_{k+1} = P_k \psi_{k+1}[\lambda + \psi_{k+1}^T P_k \psi_{k+1}]^{-1} \tag{47}$$
$$P_{k+1} = \frac{1}{\lambda}[I - K_{k+1}\psi_{k+1}^T]P_k \tag{48}$$

In this work, the parameter to be estimated is the uncertain grip coefficient $\hat{\mu}$, and the input regression term is simply the unity (49, 50).

$$\theta_k = \mu \tag{49}$$
$$\psi = 1 \tag{50}$$

The measured output (y_k) is obtained solving the expressions (39-44) for the front axle forces. The front axle lateral force (F_{yf}) is calculated from the vehicle weight distribution (51) and the front axle lateral acceleration (a_{yf}). This last term is obtained by differentiating the yaw rate and translating the lateral acceleration measured at the center of gravity to the front axle, (52).

$$F_{yf} = \frac{m l_r}{l_f + l_r} a_{yf} \tag{51}$$
$$a_{yf} = a_{y,CoG} + \dot{r} l_f \tag{52}$$

In order to determine the interpolation interval for the grip estimation, the estimated lateral force (F_{yf}) is compared to the output of the *NN* trained in the middle grip surface, $F_{y,mid}$ ($\mu = 0.6$). If the lateral force is above this threshold, the interval I_1 is considered, and expressions (39-41) are solved, obtaining (53).

$$y_k = \left(F_{yf} - \frac{\left(a_2 \hat{F}_{yfhigh,k} + b_2 \hat{F}_{yfmid,k}\right)}{a_1 \hat{F}_{yfhigh} + b_1 \hat{F}_{yfmid,k}}\right) \tag{53}$$

Conversely, if the lateral force (F_{yf}) is lower than $F_{y,mid}$, expressions (42-44) are employed, and the output y_k is calculated from expression (54).

$$y_k = \left(F_{yf} - \frac{\left(a_4 \hat{F}_{yfmid,k} + b_4 \hat{F}_{yflow,k}\right)}{a_3 \hat{F}_{yfmidh} + b_3 \hat{F}_{yflow,k}}\right) \tag{54}$$

Equation (45) is then solved recursively using the formulation (46-48). As it is typical from slip-based grip potential estimation strategies, expressions (53-54) present a singularity when the difference between forces is small. In other words, the grip identification is not reliable under straight-line or on-center driving. In order to avoid this singularity, a certain lateral dynamic threshold is introduced (55).

$$\hat{\mu}_k = \begin{cases} \hat{\mu}_k, & a_{yf} > 1.5\ m/s^2 \\ 1, & a_{yf} \leq 1.5\ m/s^2 \end{cases} \tag{55}$$

Thus, grip estimation occurs only when some difference between high and low mu forces is present, Fig. 12.

As can be noticed in Fig. 12, and has been mentioned by other authors [42], as long as the ground surface can be considered rigid with respect to the tire carcass, the tire has the same cornering stiffness regardless of the road grip coefficient. As is depicted in Fig. 12, this assertion is valid for on center driving (lateral acceleration below 1.5 m/s2).

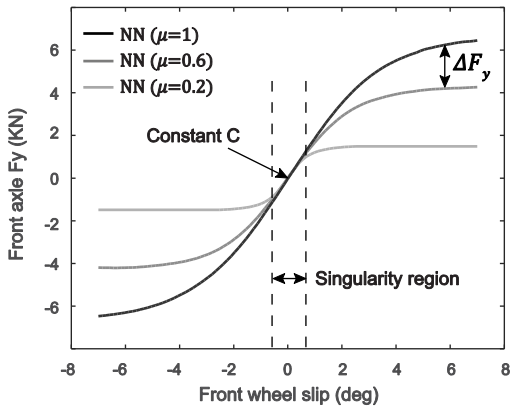

Fig. 12 NN outputs from the high, mid and low mu structures.

3.3.1. Exponential factor tuning

The exponential factor (λ) of the *RLS* block was tuned with the aim to achieve a good trade-off between noise filtering and quick parameter adaptation. The root mean square (*RMS*) of the grip error (56), and the grip consumption (57) required to pass the 10% road grip band were taken as indicators of these properties.

$$e_{\mu,RMS} = \sqrt{\frac{\sum_{k=1}^{N}\left(\hat{\mu}_k - \mu_{k,road}\right)^2}{N}} \tag{56}$$

$$grip_{cons} = \frac{abs(a_{yf})}{\mu_{road} * 9.81} \quad (57)$$

As can be noticed in Fig. 13 (a), the grip error is the minimum for an exponential factor of approximately 0.995. Higher values introduce an offset between the real and estimated signals, and the RMS error increases abruptly. Expectedly, the grip consumption required to pass the 10% road grip band increases with the exponential factor. In conclusion, a high forgetting factor (e.g. λ=0.99) reduces the signal error but requires a high lateral excitation to detect fast and abrupt changes in the road grip. On the other hand, a low forgetting factor (e.g. $\lambda = 0.97$), exhibits a faster response against abrupt changes in the road grip, but has poorer filtering capabilities.

In order to select the forgetting factor that best satisfies both requirements, the cost function (58) was constructed by adding both metrics.

$$f_{obj}(\lambda) = w_1 e_{\mu,RMS} + w_2 grip_{cons,10\%} \quad (58)$$

For simplicity, the same value was assigned to the weighting factors (w_1, w_2). The value $(\lambda = 0.97)$ was obtained after minimizing the cost function for an aggressive maneuver in $\mu = 0.7$. Several simulations were performed in roads with lower grip coefficients and best results were obtained with this exponential factor.

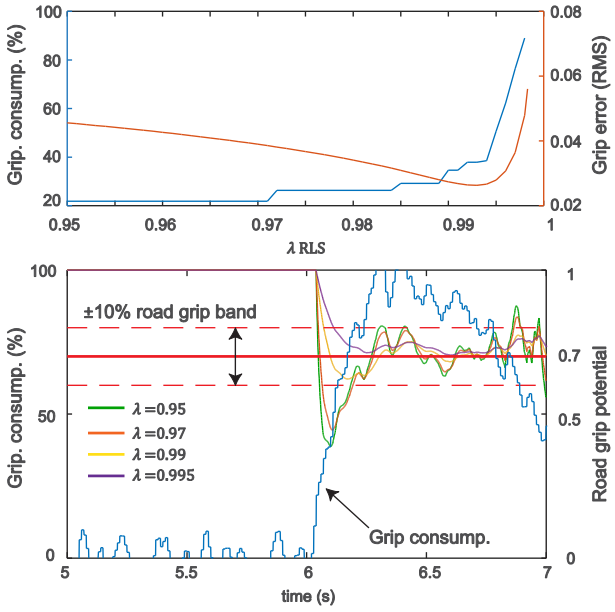

Fig. 13 (a) Grip consumption threshold and grip RMS error for different values of λ. (b) Time history of estimated grip and grip consumption for different values of λ. (Aggressive maneuver simulated in $\mu = 0.7$)

3.4. Observer implementation

The observer was constructed in *Simulink*® and integrated into the "*generic.mdl*" model of *IPG CarMaker*®. The exchange between *CarMaker*® signals was accomplished using the *CM4SL* library. The *"generic.mdl"* was simulated using a default sample time of 1ms. The observer measurements were sampled at a frequency of 100 Hz using a zero-order hold block.

$$y_{meas} = y_{CM} + w \quad (59)$$

Noise was added to the simulation signals using an additive noise model (59), where *w* represents a white Gaussian noise of variance σ^2. The yaw acceleration required to translate the lateral acceleration to the front axle was obtained using a first order discrete differentiation of the yaw rate signal. A moving average filter with an averaging period of 0.02s was used prior to the yaw rate differentiation.

Table 5. Added noise properties

Variable	Noise density	Freq. range	Variance
a_y, a_x	150 $\mu g/\sqrt{Hz}$	50 Hz	1.08e-4 $\frac{m^2}{s^4}$
v_x	-	-	7.71e-4 $\frac{m^2}{s^2}$
r	0.015 °/s/$\sqrt{Hz}$	50 Hz	3.42e-6 $\frac{rad^2}{s^2}$

The noise properties detailed in Table 5 were extracted from [43] and correspond to the specifications of the experimental equipment used during the experimental validation of the simulation model, (Fig. 6). Finally, the *Q* and *R* matrices of the Kalman filter were tuned to improve the filtering capabilities of the observer. Different weighting factors [1, 0.1, 0.01] were associated with each diagonal term of *Q* and *R*. The covariance matrices were generated using a vector combination function in *Matlab*®. In total, 243 possible combinations were tested in a Slalom maneuver simulated in *CarMaker*®.

$$Q = \begin{pmatrix} q_{yaw_r} & 0 & 0 \\ 0 & q_{v_x} & 0 \\ 0 & 0 & q_{v_y} \end{pmatrix}, \quad R = \begin{pmatrix} r_{yaw_r} & 0 \\ 0 & r_{v_x} \end{pmatrix} \quad (60)$$

$$q_{yaw_r} = 0.01, q_{v_x} = q_{v_y} = 0.1 \quad , r_{yaw_r} = r_{v_x} = 0.1$$

After computing the Normalized RMS estimation errors (61) it was observed that excessive low values of *R* tend to penalize the filtering performance of the state estimator while low values of the term q_{v_y} resulted in poor estimation of the lateral velocity when uncertainty in the tire forces was present. Finally, matrices (60) were selected after exhibiting a good compromise between noise rejection and lateral velocity accuracy.

$$e = 100 \cdot \sqrt{\frac{\sum(\hat{y}_k - y_k)^2}{N}} \cdot \frac{1}{\max(|y|)} \quad (61)$$

4. Simulation Results

The state estimator described in the previous sections was tested under different aggressive maneuvers using *IPG-Car Maker*®. The first part of this section is intended to evaluate the performance of the observer in its "reference" configuration, that is, using the vehicle and tire model employed during the

training of the *NN*. Three catalogs of maneuvers were defined to cover a wide range of scenarios: Open Loop tests, Closed Loop tests and mu-jump tests [31, 36, 44–47]. These tests are often performed in proving grounds due to their execution simplicity.

Table 6. Model configurations used during the simulations.

Configuration	Vehicle model	Tire model
Reference	Fiesta_exp	MF 205_65/R16
Ref-A	Fiesta_exp	MF 185_65/R15
Ref-B	Fiesta_exp	MF 215_50/R17
Ref-C	Fiesta_exp	MF 205_65/R16-2bar
Ref-D	Fiesta_exp	MF 205_65/R16-2.7bar
Reference-Sedan	Sedan	MF 245_40/R19
Sedan-Wet	Sedan	MF 245_40/R19 – Wet asph
Sedan-Ice	Sedan	MF 245_40/R19 – Ice

A robustness analysis is presented in the second part of the section. Simulations are carried out using tire models of different sizes (Ref-A, Ref-B), and modifying the tire operating pressure of the reference tire model (Ref-C, Ref-D). The purpose of these tests is to evaluate the suitability of the state estimator in more "realistic" scenarios, in which the uncertainties associated with the tire forces can increase due to tire replacement or lack of an adequate maintenance.

Finally, all the results presented in this paper rely on the adherence coefficient scaling approach used by the Magic Formula 6.1 [28]. In order to study the validity of this scaling method, two additional tests are simulated. The state estimator is reconstructed using a *Reference-Sedan* vehicle model and a *MF6.1 245_4/R19* tire model characterized in dry conditions ($\mu \approx 1$). The *NN* training process is repeated following the steps described in Section 3, using the tire model characterized in dry conditions and using the *MF* scaling method to approximate the tire behavior in low mu. After that, the *CarMaker*® model is equipped with two additional tire models characterized in wet asphalt and ice (*MF 245_40/R19 – Wet asph* and *MF 245_40/R19 –Ice*) and thegood performance of the observer − trained using the MF scaling method − in predicting the tire forces on these surfaces was validated.

4.1. Open loop aggressive maneuvers

In order to evaluate the observer performance under high dynamic maneuvers, several Sine with Dwell tests were executed, Table 7. It must be mentioned that active safety systems such as *ESC* or *ABS* were not considered in this evaluation.

Table 7. Open Loop catalog of maneuvers

Test	Speed/SWA/Brk*	Grip	Configuration
#1-Sine with Dwell	80/90/CD	1	Reference
#2-Sine with Dwell	80/150/CD	1	Reference
#3-Sine with Dwell	80/90/PB	1	Reference
#4-Sine with Dwell	80/90/CD	0.7	Reference
#5-Sine with Dwell	80/90/PB	0.7	Reference
#6-Sine with Dwell	80/70/CD	0.3	Reference
#7-Sine with Dwell	80/70/HB	1	Reference

*CD: Coast Down, *PB: Partial Braking, *HB: Hard Braking, MS: Maintain speed

Fig. 14 and Fig 15. show the results obtained after simulating the high mu tests. Tests (#1, #2) were performed in coasting down conditions, while a partial braking action was included in the first steering input of the third test (#3). Maneuvers involving longitudinal solicitations are not studied in the literature [3,7,9,10], where lateral dynamics estimation is restricted to constant speed situations.

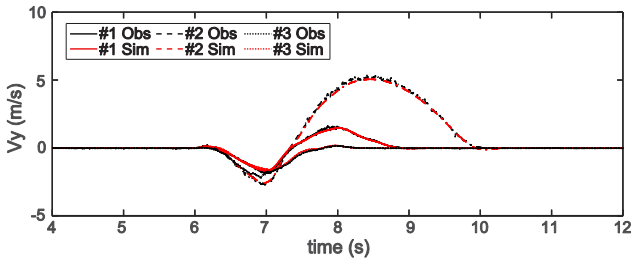

Fig. 14 Lateral velocity, tests (#1, 2).

The inclusion of longitudinal dynamics in the observer extends considerably its operating range. Overall, the estimation of lateral forces and lateral velocity is very precise. Observer performs well in moderate (#1, #3) and aggressive (#2) steering inputs. As can be noticed in Fig. 15, the front tires saturate completely during the execution of the test (#2). Despite a large slide, the lateral velocity estimation is still very accurate.

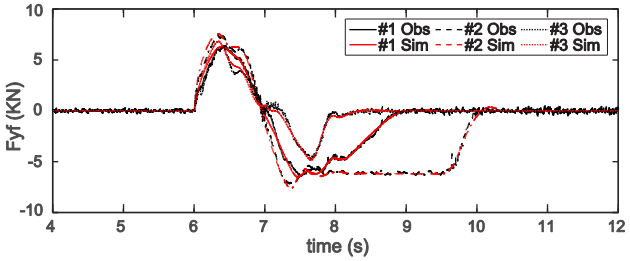

Fig. 15 Front axle lateral forces, tests (#1, 2, 3).

The same maneuvers were repeated in low mu situations (#4, #5, #6). Fig. 16 portrays the results obtained in $\mu = 0.7$ for a coast down and partial braking sine with dwell test.

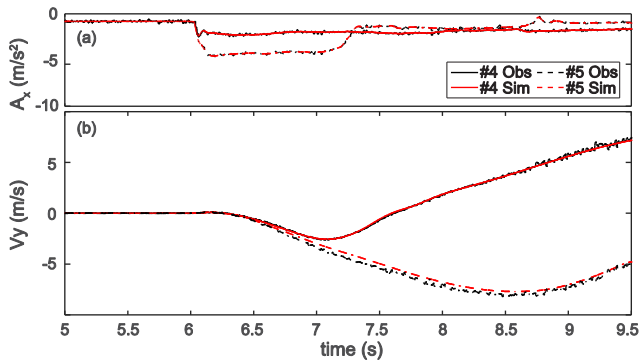

Fig. 16 (a) Longitudinal deceleration, (b) Lateral velocity. Tests (#4, 5).

In both cases (CD and PB), the vehicle exhibits an abrupt lateral slide. In the former case (#4), the front tires saturate after the second input, Fig. 17 (b), while in the latter case (#5) a large slide occurs after the first input, derived from the partial braking action, Fig. 16 (a). The *RLS* module identifies accurately the road grip potential (0.7). The first transition through the 10% road grip band occurs for a grip consumption level of 30% approximately. Despite some overshoot, the road grip estimation converges quickly to the true value, Fig. 17 (a).

Fig. 18 depicts the vehicle response after the Sine with Dwell test (#6) performed in an extreme low adherence surface ($\mu = 0.3$). As occurred in the previous case (#4), the vehicle slides laterally after the second steering input, Fig. 18 (b). The road grip estimation is remarkable, and the *RLS* module identifies the road grip potential within a 10% of accuracy for a grip consumption level of approximately 70%, Fig. 18 (a).

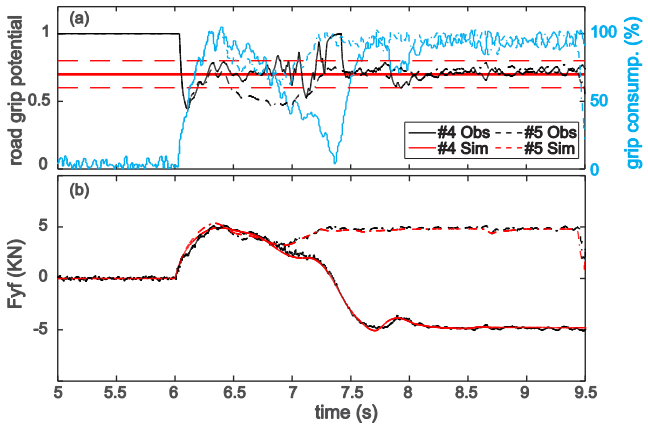

Fig. 17 (a) Estimated road grip potential, (b) Front axle lateral forces, tests (#4, 5).

The state estimator overestimates the rear axle force momentarily (around t=7s) due to the time delay between the front and rear axles (the front axle acceleration goes below the *RLS* excitation threshold and $\hat{\mu}$ switches to the default unity value while the rear axle is still generating lateral force). Despite this, the *EKF* is able to provide an accurate estimation of the lateral velocity.

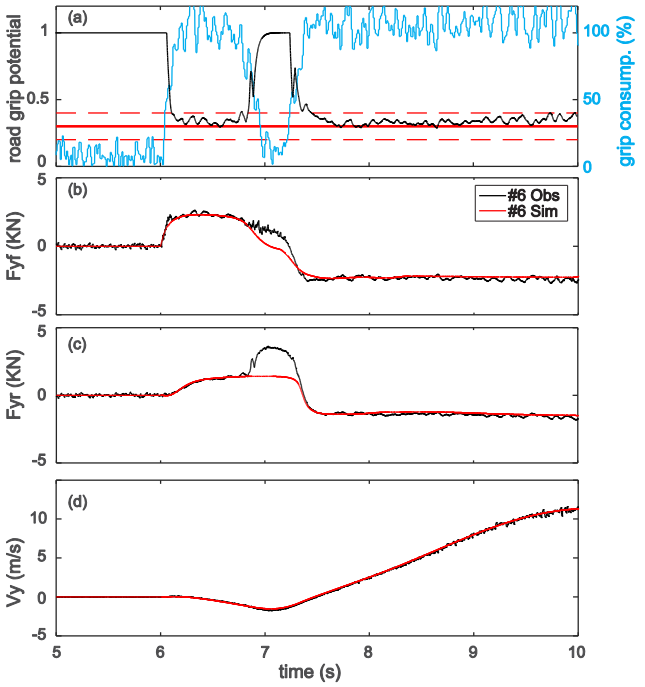

Fig. 18 (a) Estimated road grip potential, (b) Front axle lateral forces, tests (#6).

To conclude with this subsection, results from the Sine with Dwell with emergency braking (#6) are exhibited in Fig. 19. Although the driving maneuver represents a limit situation in which the full longitudinal region is covered (peak deceleration of $-9.7\ m/s^2$), and despite some inaccuracies in the front lateral force estimation, the state observer provides an acceptable estimation of the lateral velocity.

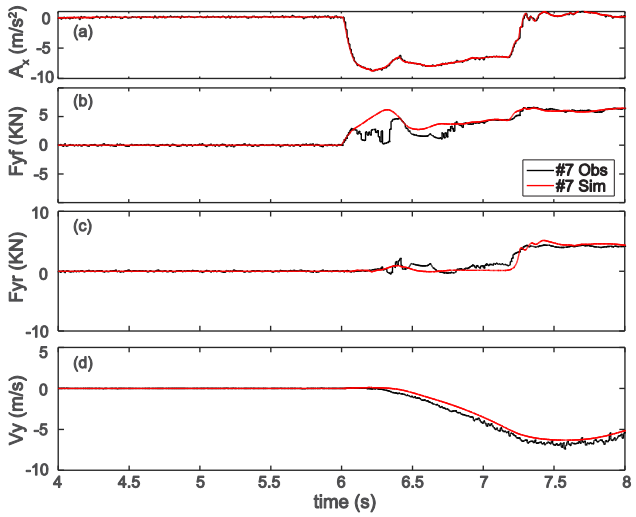

Fig. 19 (a) Longitudinal deceleration, (b) Front and (c) Rear axle lateral forces. Test (#7)

4.2. Closed loop aggressive maneuvers

Open Loop maneuvers are often interesting from a chassis characterization perspective. They are easy to perform in a proving ground and if performed with the right equipment [47] repeatability can be guaranteed. Unfortunately, real driving conditions require the interaction between the driver and the vehicle, (Closed Loop maneuvers). In order to test the algorithms proposed in this paper under more realistic and demanding conditions, the catalog of closed loop maneuvers defined in Table 8 was simulated.

Table 8. Closed Loop catalog of maneuvers

Test	Speed/SWA/Brk*	Grip	Configuration
#8-ISO LC	100/-/MS	1	Reference
#9-ADAC LC	100/-/CD	1	Reference
#10-ADAC LC	95/-/CD	0.7	Reference
#11-ADAC LC	90/-/CD	0.5	Reference
#12-Slalom 36m	80/-/MS	1	Reference
#13-Slalom 36m	65/-/MS	0.4	Reference

*CD: Coast Down, *PB: Partial Braking, *HB: Hard Braking, MS: Maintain speed

Fig. 20 depicts the results corresponding to the ISO Lane change test in high mu conditions. As can be noticed, the lateral velocity estimation is excellent, Fig. 20 (a). The axle cornering stiffnesses predicted by the state estimator are illustrated in Fig. 20 (b). Expectedly, the maximum rear wheel slip (minimum cornering stiffness) occurs when the vehicle enters the third gate of the Lane change (instant of maximum lateral velocity).

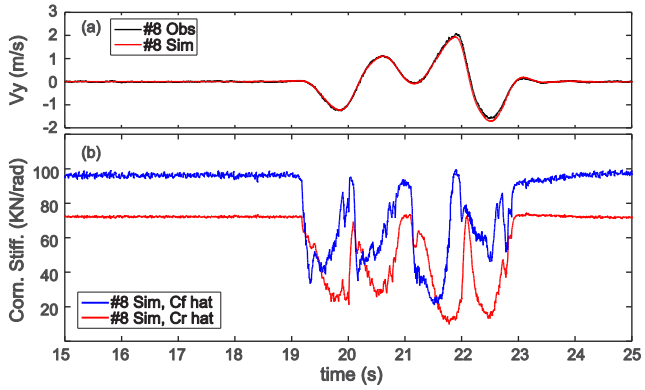

Fig. 20 (a) Lateral velocity, (b) Estimated Cornering Stiffness, Test (#8).

Fig. 21 illustrates the lateral force trajectory of the front (a) and rear axle (b) over the three-dimensional space defined by the axle sideslip, longitudinal acceleration, and axle lateral force. As can be observed in these graphs, low longitudinal acceleration is experienced during the execution of this maneuver. The forces predicted by the *NN* structure approximate well the real forces obtained in the simulation.

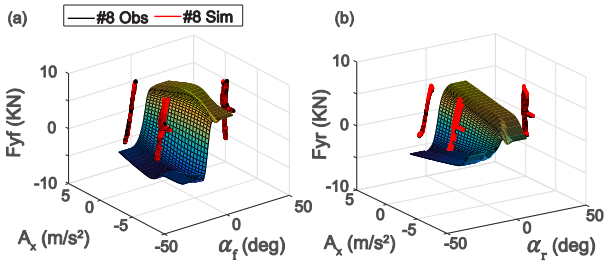

Fig. 21 NN surface estimated and simulated axle lateral forces. (a) Front axle Fy. (b) Rear axle Fy. Test (#8).

The following graphs illustrate the results obtained from the ISO ADAC (*Allgemeiner Deutscher Automobil-Club*) test, simulated in high and low mu surfaces, (#8, #9, #10). In this maneuver, the driver avoids an obstacle at high speed. The combination of low yaw damping (due to the high speed) and the phase shift between the front and rear lateral forces leads to a high yaw moment that compromises the vehicle stability [50]. The results obtained in the low mu ADAC tests (#9,#10) are presented in Fig. 22 and Fig. 23. The performance of the state estimator in these scenarios is of vital importance in order to guarantee an early recognition of a low adherence situation. In the first test ($\mu = 0.7$), the *RLS* block detects an abrupt change in road grip potential and passes the 10% threshold for a grip consumption of 40% approximately, Fig. 22 (a).

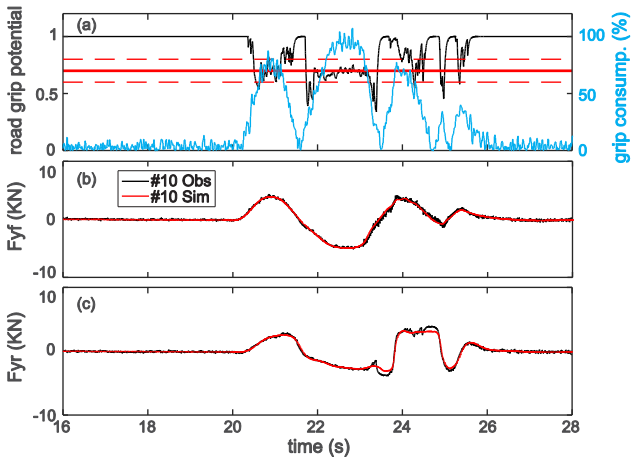

Fig. 22 (a) Estimated road grip potential, (b) Lateral velocity. Test (#10).

Fig. 23 portrays the results obtained simulating the vehicle in a surface with an adherence coefficient of 0.5. In this case, the grip potential is recognized within a 10% accuracy for a grip consumption level of roughly 50%. The state estimator approximates precisely the lateral velocity obtained in the simulation model, Fig. 23 (b). These results are promising, evidencing the ability of the observer to estimate the lateral velocity in aggressive maneuvers executed over low mu surfaces.

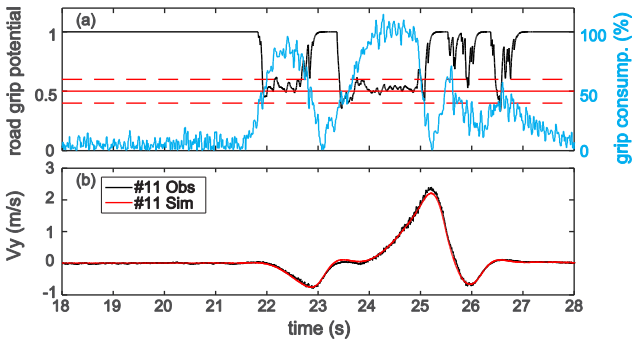

Fig. 23 (a) Estimated road grip potential, (b) Front and (c) Rear axle lateral forces, Test (#11).

To conclude with this subsection, Slalom tests are simulated in high and extremely low friction surfaces (#10, 11). This maneuver (either 18 or 36m) is often used to evaluate the vehicle agility and does not represent a serious stability issue. However, zero force transitions occur continuously and the mu recognition algorithm can be affected by the singularities described in Section 3.3. Thus, it is a good scenario to test the performance of the observer. Fig. 24 shows the grip (a), axle lateral forces (b, c), and lateral velocity (d) estimated by the state estimator and *RLS* block. Overall, the performance of the observer is good. Some peaks above the unity are observed in the estimated grip after each steering cycle completion. In order to avoid extrapolation issues, a saturation block is employed to keep the grip input ($\hat{\mu}$) within the limits defined in Section 3.2.3.

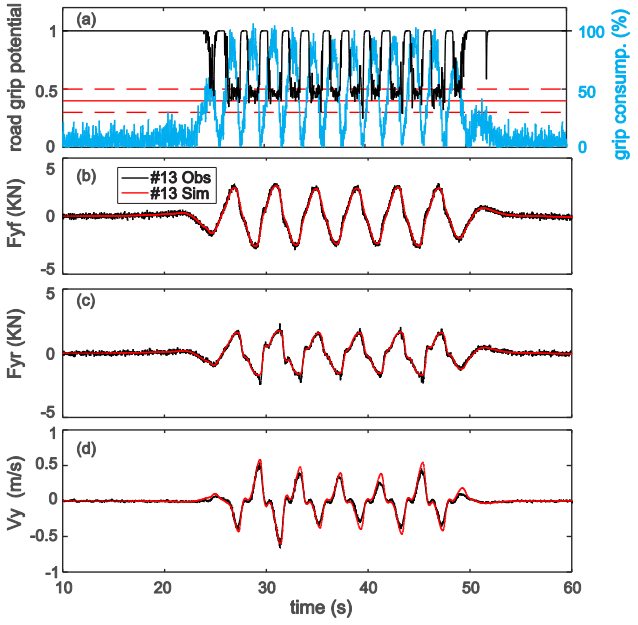

Fig. 24 (a) Estimated road grip potential, (b, c) axle lateral forces, (d) lateral velocity. Test (#13).

4.3. Mu-jump maneuvers

The tests described in the previous subsections share a common point: the grip coefficient of the road does not vary during the maneuver execution. Thus, in order to evaluate the state estimator response under grip transitions (often called mu-jump situations) two additional scenarios were simulated (Table 9).

Table 9. Mu-jump catalog of maneuvers

Test	Speed/SWA/Brk*	Grip	Config.
#14-Straight Line μ-jump	100/-/MS	0.8-0.6-0.4-0.2	Reference
#15-Circle μ-jump	50/R50/MS	0.8-0.4	Reference

*CD: Coast Down, *PB: Partial Braking, *HB: Hard Braking, MS: Maintain speed

The first test (#14) consists of a set of mu transition (0.8-0.6-0.4-0.2) executed at a constant speed. Low frequency (0.2Hz) sine steering inputs are applied continuously during the test.

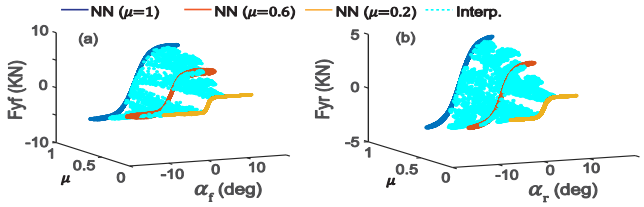

Fig. 25 (a) Front axle lateral forces. (b) Rear axle lateral forces, Test (#14).

The interpolation surfaces of the axle lateral forces are showed in Fig. 25. As can be appreciated in Fig.26 (a), the performance of the observer is remarkable during the consecutive surface transitions, and the grip potential of the road is well identified at each surface.

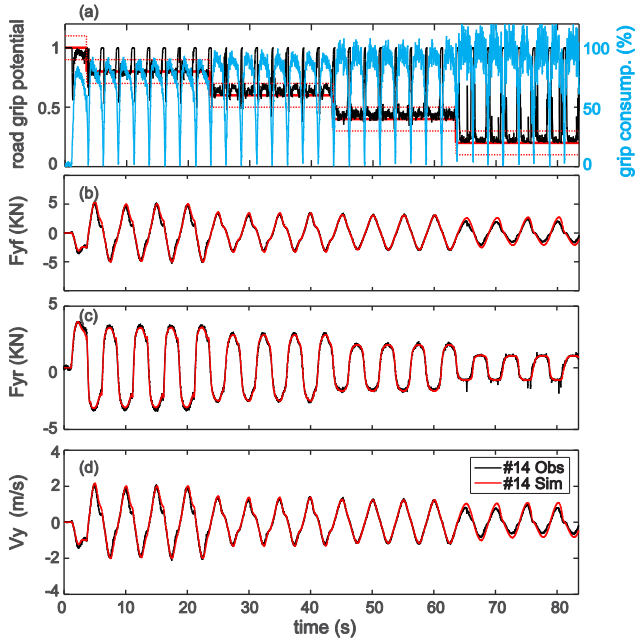

Fig. 26 (a) Estimated road grip potential, (b, c) axle lateral forces, (d) lateral velocity. Test (#14).

The probability distribution of the grip estimated at each surface is presented in Fig. 27.

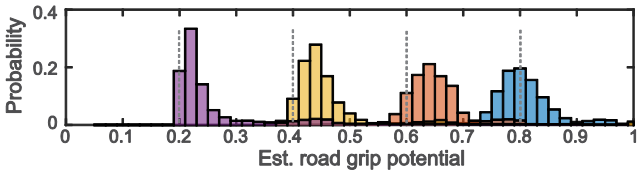

Fig. 27 Probability distributions computed from the road estimated grip. Test (#14). Bins limits [0.05 1], Bin width 0.02.

The average grip consumption levels required to pass the 10% road grip potential band are summarized in Table 10.

Table 10. Grip consumption levels for a detection of the road grip potential with an accuracy of the 10%.

Mu coefficient	0.8	0.6	0.4	0.2
Grip cons. level 10%	25%	40%	50%	85%

Overall, the grip consumption values remain below the 85% - 90% levels required by pure lateral force-slip regression methods [52]. Other grip identification methods (Moment-slip regression) can provide accurate estimates for excitation levels of 30, 40% [52], but their suitability under longitudinal excitation has not been covered in detail in the literature [22,24]. The approach presented in this paper lies between these excitation levels and presents a certain robustness against longitudinal solicitations. Thus, this state estimator is proposed as an efficient way to infer the road grip potential under intermediate driving situations. A hybrid structure such as introduced in [53], can be employed to achieve a continuous grip potential identification, combining pure longitudinal and lateral slip-based observers with this state estimator.

Finally, to conclude with the observer evaluation in its reference configuration, a constant radius mu-jump test (#15) is simulated. The estimation of the vehicle states during this maneuver is often difficult due to the low dynamics involved (slow body-slip estimation). Any mismatch in the state estimation can lead after some seconds to large drifts in the estimated signals. During each turn, the vehicle passes through three low mu segments Fig.28. The vehicle moves counter-clockwise, and a negative increase in the lateral velocity is expected caused by the abrupt grip reduction (vehicle slides towards the outer hard shoulder due to the centripetal force).

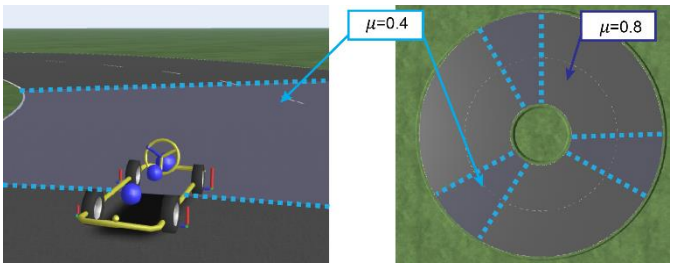

Fig. 28 Mu-split circle modeled in Car Maker. Test (#15).

The estimated lateral velocity is depicted in Fig. 29 (b). Expectedly, the vehicle slides to the outer track limit at each low mu transition (negative lateral velocity). Abrupt changes in the road grip are well identified by the *RLS* block at each transition, Fig. 29 (a).

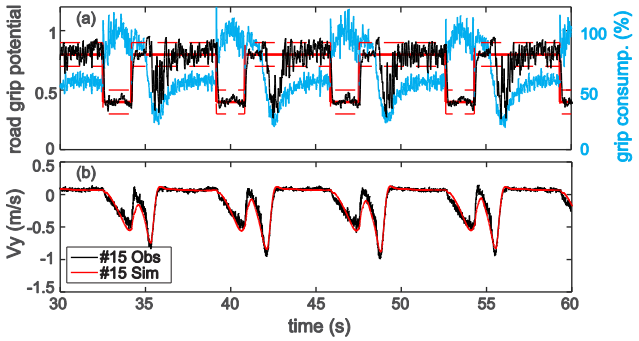

Fig. 29 (a) Estimated road grip potential, (b) Lateral velocity. Test (#15).

The axle cornering stiffnesses estimated by the state estimator are depicted in Fig. 30. At each high-to-low mu-jump, the cornering stiffness drops to almost zero, and the tires saturate, Fig. 30.

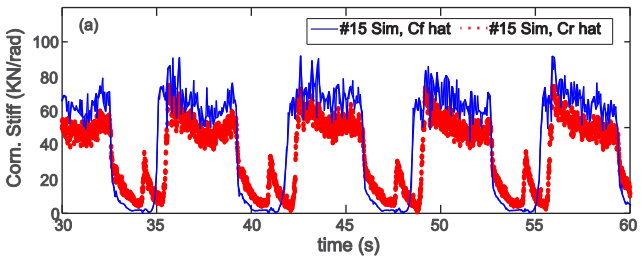

Fig. 30 (a) Estimated road grip potential, (b) Estimated axle cornering stiffness. Test (#15).

Estimates of the yaw rate and longitudinal velocity are showed in Fig. 31. The peaks in the yaw rate after each mu transition are provoked by the low-to-high mu-jump. The front axle recovers grip first and creates a positive yaw moment on the chassis.

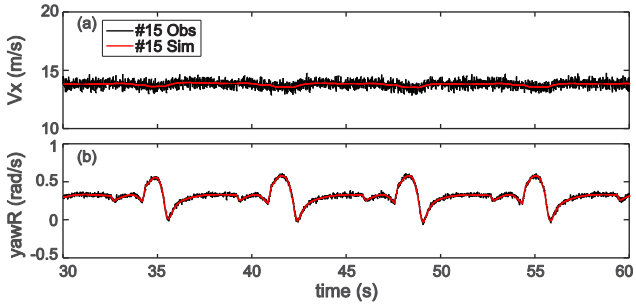

Fig. 31 (a) Longitudinal velocity, (b) Yaw rate. Test (#13).

The same peaks are observed in the axle forces Fig. 32, each time the front axle recovers grip.

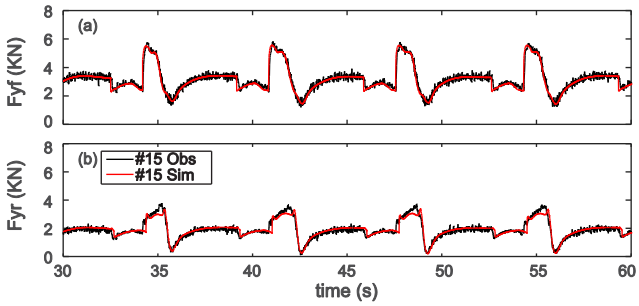

Fig. 32 (a) Estimated front axle force, (b) Estimated rear axle force, Test (#13).

4.4. Observer Robustness analysis

Up to now, the state estimator has performed well when the reference configuration has been employed (the same tire model used to train the *NN* has been employed during the simulations). In the following subsection, the robustness of the observer against variations in the tire size and tire operating pressure is tested. The tests presented in Table 11 were performed using the vehicle configurations detailed in Table 6. The first configurations (Ref-A, Ref-B) correspond to variations in the tire size (R15, R17 respectively) and the third and fourth configurations (Ref-C, Ref-D) indicate variations in the tire operating pressure of the reference tire. In order to have a precise simulation of the tire forces, the pressure variations are kept within the limits imposed by the tire model ($\mp 0.4\ bar$). Pressure values out of this range are not considered in this paper, assuming a fault detection of the Tire Pressure Monitoring System (*TPMS*) and the subsequent reestablishment of the nominal pressure.

Table 11. Catalog of maneuvers to evaluate the robustness of the observer.

Test	Speed/SWA/Brk*	Grip	Configuration
#16-Sinus with Dwell	80/150/CD	1	Ref-A
#17-Sinus with Dwell	80/150/CD	1	Ref-B
#18-Sinus with Dwell	80/90/CD	0.7	Ref-A
#19-Sinus with Dwell	80/90/CD	0.7	Ref-B
#20-ADAC LC	70/-/CD	0.5	Ref-C
#21-ADAC LC	70/-/CD	0.5	Ref-D

*CD: Coast Down, *PB: Partial Braking, *HB: Hard Braking, MS: Maintain speed

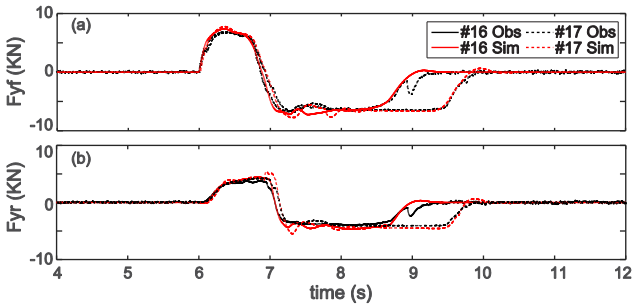

Fig. 33 (a). Estimated front axle force, (b) Estimated rear axle force, Test (#16, #17).

The results concerning the high mu tests (#16, #17) are presented in Fig. 33. As occurred in the evaluation of the reference model, the tires saturate after the second steering input. The accuracy of the observer is remarkable in spite of the use of a tire model of different size.

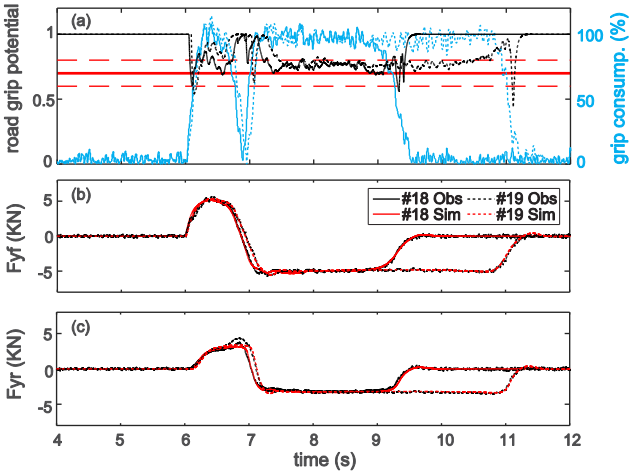

Fig. 34 (a). Estimated road grip potential, (b) front axle force, (c) rear axle force, Test (#18, #19).

Fig. 34 depicts the results obtained after performing the simulations on a road with an adherence coefficient of 0.7. The *RLS* block identifies an abrupt change in road grip potential during the first steering input for an approximate excitation level of 30%. The estimated grip presents a slight offset due to the different characteristics of the new tires, but the estimation of the axle lateral forces is still very accurate.

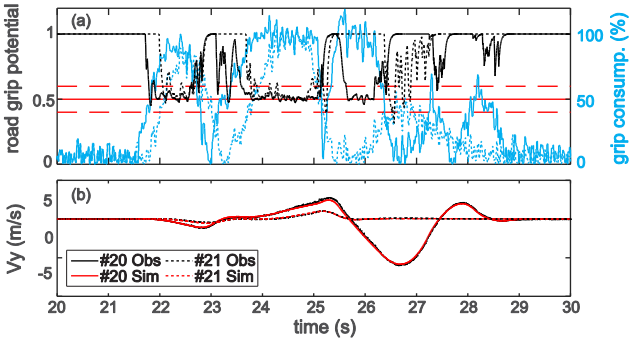

Fig. 35 (a). Estimated road grip potential, (b) Estimated lateral velocity, Test (#20, #21).

Finally, results concerning the variations in tire operating pressure (#20, #21) are shown in Fig. 35. In both cases, the low mu condition is identified by the *RLS* block during the first steering input ($t \approx 21.5$), Fig. 35 (a). In addition, the lateral velocity predicted by the state estimator approximates very well the values obtained in the simulation.

The results provided in this section are promising in what concerns the robustness of the state estimator against modifications in the reference configuration. Although more tests are to be performed to fully determine the operating limits of the observer, it seems that the flexibility of the approach presented in this paper may be suitable to predict the behavior of a certain number of vehicle configurations, thus avoiding the observer re-calibration and *NN* training for each individual vehicle variant.

4.5. Validation of the Magic Formula grip scaling approach

To conclude with this section, two additional tests are presented with the aim to validate the low mu scaling approach used in the MF tire model [28]. A tire of size *245_40/R19* was characterized in three different surfaces (dry-$\mu \approx 1$, wet asphalt-$\mu \approx 0.9$ and ice-$\mu \approx 0.35$) and a MF 6.1 model was obtained for each adherence condition.

Table 12. Catalog of maneuvers to evaluate the validity of the Magic Formula grip scaling approach.

Test	Speed/SWA/Brk*	Grip	Configuration
#22-Sinus with Dwell	80/120/CD	0.90	Sedan-Wet
#23-Sinus with Dwell	80/40/CD	0.35	Sedan-Ice

*CD: Coast Down, *PB: Partial Braking, *HB: Hard Braking, MS: Maintain speed

A comparison between the curves scaling the model parameterized in dry conditions and the curves determined after testing the tire in wet asphalt and ice is presented in Fig. 36.

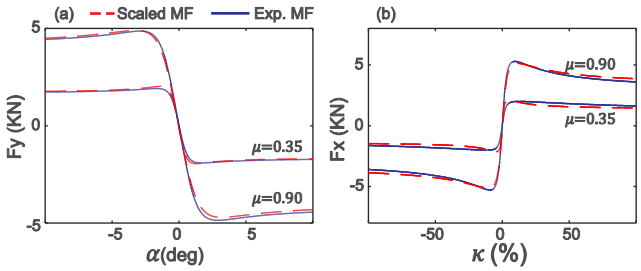

Fig. 36 (a). Pure lateral force, (b) pure longitudinal force from wet asphalt and ice surfaces. Tire size: 245_40/R19.

Due to the new limitations imposed by the tire data available, the state estimator was updated taking the parameters of a sedan vehicle model and the *NN* structure was retrained using the tire model characterized in dry conditions. (Additional details regarding the tire and vehicle model employed during the simulations are omitted for confidentiality reasons.)

The tests presented in Table 12 were simulated to evaluate the suitability of the MF grip scaling approach. This time, instead of modifying the road grip coefficient in *IPG-Car Maker®*, the tire models obtained experimentally were used.

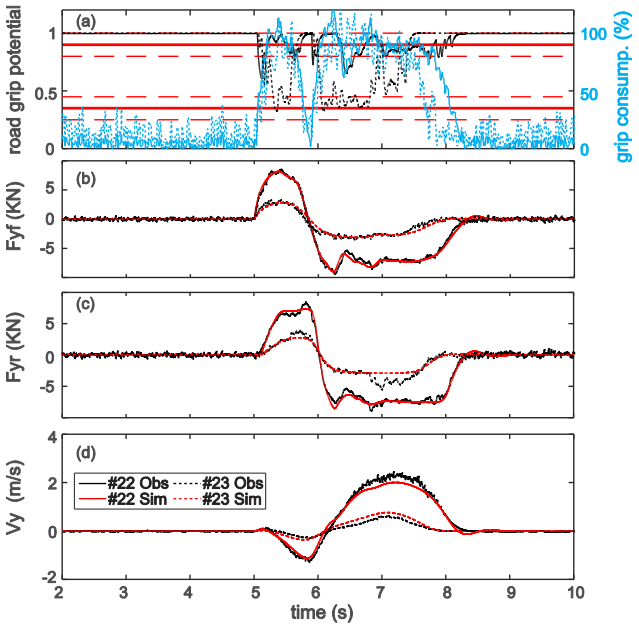

Fig. 37 (a). Estimated road grip potential, (b) front axle force, (c) rear axle force, (d) lateral velocity. Tests (#22, #23).

The results of these simulations are depicted in Fig. 37. In both cases (wet asphalt, #22 and ice, #23) the performance of the state estimator is good. The estimated forces follow accurately the simulation forces Fig. 37 (b, c) and the road grip potential is identified correctly, Fig. 37 (a).

4.6. Metrics

In order to evaluate the performance of the proposed observer, a set of metrics were defined and calculated after each simulation completion. Table 13 contains the metrics corresponding to the tests presented during this section, Tables 7, 8, 9, 11, and 12. The normalized root mean square error [7] defined in expression (61) was chosen to evaluate the error of the estimated states. In total, 5 metrics were defined: longitudinal velocity e_{vx}, yaw rate e_r, lateral velocity e_{vy}, front axle lateral force e_{Fyf} and rear axle lateral force e_{Fyr} estimation error. Overall, small errors are observed in the states estimated by the *EKF* (in majority of tests values are kept below a 5% error threshold). Lowest errors are found in the states that are measured directly by the *EKF* (yaw rate and longitudinal velocity). Concerning lateral velocity, a maximum error of 6.80% is obtained in test #23 due to the low lateral excitation observed in icy conditions. Nevertheless, this value remains well below the 10% threshold and can be considered acceptable.

Table 13. Error metrics

Test	e_{v_x}	e_r	e_{v_y}	$e_{F_{yf}}$	e_{Fyr}
#1	1.19	2.45	2.83	2.78	5.05
#2	1.19	1.63	2.98	3.27	5.14
#3	1.18	2.84	5.30	3.68	9.11
#4	1.20	1.56	1.14	2.79	5.24
#5	1.18	1.51	4.46	2.88	5.75
#6	1.20	2.25	0.63	8.99	23.60
#7	1.20	0.99	4.95	11.27	6.41
#8	0.94	2.76	1.56	1.92	2.86
#9	0.94	3.22	2.44	1.94	3.14
#10	1.00	1.55	0.86	3.14	5.01
#11	1.05	2.52	1.19	3.81	9.23
#12	1.18	5.89	4.85	2.80	4.41
#13	1.32	6.29	5.12	5.55	6.87
#14	1.16	3.55	6.47	4.91	3.90
#15	1.32	2.63	7.50	4.27	6.54
#16	1.19	1.76	9.53	5.82	7.44
#17	1.19	1.51	5.87	4.47	6.44
#18	1.19	2.78	3.28	2.52	4.16
#19	1.20	2.41	2.10	2.77	4.27
#20	1.05	1.35	1.00	6.85	16.58
#21	1.06	3.82	2.48	3.40	6.37
#22	1.36	2.43	5.37	3.18	4.30
#23	1.39	7.10	8.73	8.77	14.49

Finally, axle lateral force errors kept within reasonable limits during the majority of the simulations. Large errors are found in the rear axle forces during the execution of tests #6 and #20. These tests correspond to aggressive maneuvers executed in low mu conditions. As was observed in Fig. 18, the delay between the front and rear axle can cause a momentary overestimation of the rear axle forces, which contributes to increasing significantly the estimation error. Despite this, the *EKF* is able to correct these inaccuracies and the vehicle states are predicted with high accuracy.

5. Conclusions

An innovative *tire model-less* method to estimate with high accuracy the vehicle lateral dynamics and tire-road friction forces under aggressive maneuvers has been proposed. The main advantage of this method is that it avoids the complex and costly tire modeling task, bypassing this step by training a Neural Network structure using repeatable data from Step Steer maneuvers. An important contribution of this work is that partial and hard braking events have been included in the training dataset with the objective to cover a wide range of critical driving scenarios. In addition, the Feedforward structure is trained with data from *full-vehicle level* tests. These data already contain information regarding the tire-chassis interaction, e.g. suspension kinematics, so it is not necessary to model these suspension effects in the state estimator and the model complexity can be kept low.

The vehicle dynamic equations and first order tire model have been integrated forming a hybrid structure composed of an Extended Kalman Filter and a Neural Network structure. A Recursive Least Squares block completes the state estimator with the aim to monitor the road grip potential and corrects the tire forces predicted by the Neural Network structure. The observer has been modeled in *Simulink*® and simulations have been carried out using the vehicle dynamics software *IPG Car Maker*® using a parameterized experimental vehicle. White Gaussian Noise based on the specifications of the testing instrumentation has been added to the simulation signals in order to evaluate the filtering capabilities of the *EKF*. A wide range of objective testing maneuvers (open loop, closed loop, and mu-jump) have been simulated in different vehicle configurations, including tire size variations and modifications in the tire operating pressure. In addition, the validity of the grip scaling approach employed by the MF 6.1 has been evaluated using tire models parameterized in dry, wet asphalt and ice surfaces.

The graphs and metrics presented in the previous section demonstrate the remarkable performance of the state estimator under aggressive maneuvers in high and low adherence conditions. Discussion regarding the grip consumption levels required to detect abrupt changes in the road grip potential has been provided. The experimental validation of the state estimator in a Proving Ground will be pursued during the next steps of this research. Additionally, the integration of the observer with pure longitudinal and lateral slip-based grip estimators will be studied in the future.

Acknowledgements

"This project is part of the Interdisciplinary Training Network in Multi-Actuated Ground Vehicles (ITEAM) European program and has received funding from the European Union's Horizon 2020 research and innovation program under the Marie Skłodowska-Curie grant agreement No 675999."

Conflict of interest:

The authors declare that they have no conflict of interest.

References

1. Zanten A Van (2002) Evolution of Electronic Control Systems for Improving the Vehicle Dynamic Behavior. Int. Symp. Adv. Veh.

Control

2. Chakraborty I, Tsiotras P, Lu J (2011) Vehicle posture control through aggressive maneuvering for mitigation of T-bone collisions. In: Proc. IEEE Conf. Decis. Control. pp 3264–3269
3. Gao X (2010) Nonlinear Estimation of Vehicle Sideslip Angle Based on Adaptive Extended Kalman Filter. SAE Tech Pap. doi: 10.4271/2010-01-0117
4. Hrgetic M, Deur J, Ivanovic V, Tseng E (2014) Vehicle Sideslip Angle EKF Estimator based on Nonlinear Vehicle Dynamics Model and Stochastic Tire Forces Modeling. SAE Int J Passeng Cars - Mech Syst. doi: 10.4271/2014-01-0144
5. Boada BL, Garcia-Pozuelo D, Boada MJL, Diaz V (2016) A Constrained Dual Kalman Filter Based on pdf Truncation for Estimation of Vehicle Parameters and Road Bank Angle: Analysis and Experimental Validation. IEEE Trans Intell Transp Syst 1–11. doi: 10.1109/TITS.2016.2594217
6. Jiang K, Victorino AC, Charara A, et al (2015) Adaptive Estimation of Vehicle Dynamics Through RLS and Kalman Filter Approaches. In: IEEE Int. Conf. Intell. Transp. Syst. pp 1741–1746
7. Doumiati M, Charara A, Victorino A, Lechner D (2012) Vehicle Dynamics Estimation using Kalman Filtering. doi: 10.1002/9781118578988
8. Antonov S, Fehn A, Kugi A (2011) Unscented Kalman filter for vehicle state estimation. Veh Syst Dyn 49:1497–1520. doi: 10.1080/00423114.2010.527994
9. Stéphant J, Charara A, Meizel D (2005) Evaluation of sliding mode observer for vehicle sideslip angle. IFAC Proc Vol 16:150–155. doi: 10.1016/j.conengprac.2006.04.002
10. Baffet G, Charara A, Lechner D (2009) Estimation of vehicle sideslip, tire force, and wheel cornering stiffness. Control Eng Pract 17:1255–1264. doi: 10.1016/j.conengprac.2009.05.005
11. Wilkin M, Crolla DC, Levesley MC, Manning WJ (2004) Estimation of Non-Linear Tyre Forces for a Performance Vehicle using an Extended Kalman Filter. SAE Tech Pap. doi:10.4271/2004-01-3529
12. Ray R (1997) Nonlinear Tire Force Estimation and Road Friction Identification : Simulation and Experiments *. Automatica 33:1819–1833.
13. Yang J, Chen W, Wang Y (2014) Estimate Lateral Tire Force Based on Yaw Moment without Using Tire Model. Hindawi. doi: 10.1155/2014/934181
14. Albinsson A, Bruzelius F, Jonasson M (2014) Tire Force Estimation Utilizing Wheel Torque Measurements and Validation in Simulations and Experiments. In: Int. Symp. Adv. Veh. Control. pp 294–299
15. Cho W, Yoon J, Yim S, et al (2003) Estimation of tire forces for application to vehicle stability control. IEEE Trans Veh Technol 59:638–649.
16. Nam K, Oh S, Fujimoto H, Hori Y (2013) Estimation of sideslip and roll angles of electric vehicles using lateral tire force sensors through RLS and kalman filter approaches. IEEE Trans Ind Electron 60:988–1000. doi: 10.1109/TIE.2012.2188874
17. Hrgetic M, Deur J, Pavkovic D, Barber P (2011) Adaptive EKF Based Estimator of Sideslip Angle Using Fusion of Inertial Sensors and GPS. SAE Int J Passeng Cars - Mech Syst 4:700–712. doi: 10.4271/2011-01-0953
18. Croft-white M (2006) Measurement and Analysis of Rally Car Dynamics at High Attitude Angles. Ph.D. Thesis, Cranf. Univ.
19. Klier W, Reim A, Stapel D (2008) Robust Estimation of Vehicle Sideslip Angle -- An Approach w/o Vehicle and Tire Models. Proc SAE World Congr. doi: 10.4271/2008-01-0582
20. Melzi S, Sabbioni E (2011) On the vehicle sideslip angle estimation through neural networks: Numerical and experimental results. Mech Syst Signal Process 25:2005–2019. doi: 10.1016/j.ymssp.2010.10.015
21. Sasaki H, Nishimaki T (2000) SAE TECHNICAL A Side-Slip Angle Estimation Using Neural Network for a Wheeled Vehicle. doi: 10.4271/2000-01-0695
22. Matilainen MJ, Tuononen AJ (2011) Tire friction potential estimation from measured tie rod forces. IEEE Intell Veh Symp Proc 320–325. doi: 10.1109/IVS.2011.5940528
23. Mántaras DA, Luque P, Nava JA, Riva P (2013) Tyre – road grip coefficient assessment . Part 1 : off-line methodology using multibody dynamic simulation and genetic algorithms. Veh Syst Dyn 51:1603–1618. doi: 10.1080/00423114.2013.818157
24. Luque P, Mántaras DA, Fidalgo E, et al (2013) Tyre – road grip coefficient assessment – Part II : online estimation using instrumented vehicle , extended Kalman filter , and neural network. Veh Syst Dyn 51:1872–1893. doi: 10.1080/00423114.2013.841963
25. Yasui Y, Tanaka W (2004) Estimation of Lateral Grip Margin Based on Self-aligning Torque for Vehicle Dynamics Enhancement. SAE World Congr. doi: 10.4271/2004-01-1070
26. Edelmann J, Gobbi M, Mastinu G, et al (2015) Friction Estimation at Tire-Ground Contact Manfred Ploechl. SAE Int J Passeng Cars - Mech Syst. doi: 10.4271/2015-01-1594
27. Hahn JO, Rajamani R, Alexander L (2002) GPS-based real-time identification of tire-road friction coefficient. IEEE Trans Control Syst Technol 10:331–343. doi: 10.1109/87.998016
28. Pacejka HB (2012) Tire and Vehicle Dynamics. Butterworth – Heinemann. doi: 10.2307/3885338
29. Velenis E, Tsiotras P, Canudas-de-Wit C, Sorine M (2005) Dynamic tire friction models for combined longitudinal and lateral vehicle motion. Veh Syst Dyn 43:3–29. doi: 10.1080/00423110412331290464
30. Milliken WF, Milliken DL (1995) Race Car Vehicle Dynamics. SAE Int. doi: 1560915269
31. ISO (2011) ISO - 7401, Road vehicles, lateral transient response test methods, Open-loop test methods.
32. Kanarachos S (2012) A new min-max methodology for computing optimized obstacle avoidance steering maneuvers of ground vehicles. Int J Syst Sci 7721:1–16. doi: 10.1080/00207721.2012.745020
33. Psichogios DC, Ungar LH (1992) A hybrid neural network first principles approach to process modeling. AIChE J 38:1499–1511. doi: 10.1002/aic.690381003

34. Kiencke U, Nielsen L (2005) Automotive control systems: For engine, driveline, and vehicle. Springer. doi: 10.1007/b137654
35. Belic I (2012) Neural Networks and Static Modelling. Neural Networks Static Model. Recurr. Neural Networks Soft Comput. Dr. Mahmoud ElHefnawi
36. ISO (2006) ISO - 7975, Passenger Cars, Braking in a Turn, Open Loop test.
37. Beale MH, Hagan M, Demuth H (2016) Neural Network toolbox User's Guide. Mathworks
38. Liang C, Allen RW, Rosenthal TJ, Chrstos JP (2004) Tire Modeling for Off-Road Vehicle Simulation. SAE Tech Pap. doi: 10.4271/2004-01-2058
39. Lee JH, Liu Q, Zhang T (2005) Predictive Semi-Analytical Model for Tire-Snow Interaction Reprinted From : Military Vehicle Technology. SAE Tech Pap. doi: 10.4271/2005-01-0932
40. Allen RW, Rosenthal TJ, Chrstos JP (2014) A Vehicle Dynamics Tire Model for Both Pavement and Off-Road Conditions. SAE Tech Pap. doi: 10.4271/970559
41. Young P (2011) Recursive Estimation and Time-Series Analysis. Springer
42. Tavernini D, Massaro M, Velenis E, et al (2013) Minimum time cornering: the effect of road surface and car transmission layout. Veh Syst Dyn Int J Veh Mech Mobil 51:1533–1547. doi: 10.1080/00423114.2013.813557
43. RaceLogic (2013) Inertial measurement unit Data.
44. ISO (2012) ISO - 4138, Road vehicles, Steady State circular driving behavior.
45. ISO (2010) ISO - 13674, Road vehicles, Test methods for quantification of on-centre handling.
46. ISO (1999) ISO - 3888, Road vehicles, Test track for a severe lane-change maneuver.
47. UNECE (2014) Regulation No. 13 H, Uniform provisions concerning the approval of passenger cars with regard to braking.
48. Svendenius J (2007) Tire modeling and Friction Estimation, Ph.D Thesis. Department of Automatic Control, Lund University, Sweden
49. Tuononen A (2009) Vehicle Lateral State Estimation Based on Measured Tyre Forces. Sensors. 9(11):8761–8775. doi: 10.3390/s91108761
50. Acosta M, Kanarachos S, Blundell M (2016) Vehicle Agile Maneuvering: From Rally Drivers to a Finite State Machine Approach. IEEE International Symposium on Computational Intelligence.
51. Singh K, Their S (2014) Estimation of tire-road friction coefficient and its application in chassis control systems. Systems Science and Control Engineering. 3(1):38-61. doi: 10.1080/21642583.2014.985804
52. Gray A, Gao Y, Lin T, Hedrick J, Tseng H, Borrelli F (2012) Predictive Cotnrol for Agile Semi-Autonomous Ground Vehicles using Motion Primitives. American Control Conference.
53. Ahn C (2011) Robust Estimation of road friction coefficient, Ph.D Thesis, University of Michigan, USA.
54. The Multi-Body Systems Approach to Vehicle Dynamics. M. Blundell, D. Harty.
55. Kanarachos, S. (2013). Design of an intelligent feed forward controller system for vehicle obstacle avoidance using neural networks. International Journal of Vehicle Systems Modelling and Testing, 8(1), p.55-87.
56. Kanarachos, S. and Kanarachos, A. (2015). Intelligent road adaptive suspension system design using an experts' based hybrid genetic algorithm. Expert Systems with Applications, 42(21), pp.8232-8242.

Nomenclature

T_s	Discretization time
v_x	Longitudinal velocity
v_y	Lateral velocity
r	Yaw rate
m	Vehicle total mass (Sprung + unsprung)
δ	Average normalized steering angle
$F_{yf,r}$	Axle lateral forces
$F_{xf,r}$	Axle longitudinal forces
I_z	Yaw inertia
$l_{f,r}$	Longitudinal distance to center of gravity
U	Vector of inputs
Y	Vector of outputs
X	Vector of states
$\alpha_{f,r}$	Axle wheel slip
$\lambda_{f,r}$	Axle longitudinal slip
F_{y0}	Equilibrium lateral force
$\Delta\alpha$	Axle wheel slip increment
$\Delta\lambda$	Axle longitudinal slip increment
C	Axle Cornering stiffness
$\Delta\alpha_t$	Axle wheel slip differentiation increment
a_x	Longitudinal acceleration
a_{yf}	Front axle lateral acceleration
$F_{yf,rhigh}$	NN High mu lateral force estimate
$F_{yf,rlow}$	NN Low mu lateral force estimate
μ	Road adherence coefficient
w	Process white gaussian noise
v	Measurement white gaussian noise
$f(\cdot)$	State evolution vector
$h(\cdot)$	Observation vector
A	State vector Jacobian
P	Covariance matrix (Kalman filter, RLS)
Q	Process noise covariance matrix
R	Measurement noise covariance matrix
H	Observation vector jacobian
L_f^r	$r-th$ Lie derivative of vector field f
x_0	Equilibrium state
Z	Vector of system parameters
a_i	Artificial neuron inputs
a_j	Artificial neuron output
$W_{i,j}$	Artificial neuron weights
S_j	Artificial neuron output, previous to activation function
F_z	Axle vertical load
h_{CoG}	Center of gravity height

$\dot{r}$	Yaw acceleration
$a_{y,CoG}$	Lateral acceleration at the center of gravity
λ_e	Forgetting factor, RLS
ψ	Vector of Input regressors, RLS
θ	Vector of estimated parameters, RLS
y_{meas}	Measured variable
y_{CM}	CarMaker variable
N	Length of time-history